Available online at www.sciencedirect.com

ScienceDirect

Geochimica et Cosmochimica Acta 273 (2020) 1–25

Geochimica et Cosmochimica Acta

www.elsevier.com/locate/gca

Examination of crystal dissolution in 3D: A way to reconcile dissolution rates in the laboratory?

Catherine Noiriel [a,*], Matthias Oursin [a], Damien Daval [b]

[a] *Géosciences Environnement Toulouse, Observatoire Midi-Pyrénées, Université Paul Sabatier, CNRS, IRD, Université de Toulouse, 14 avenue Edouard Belin, F-31400 Toulouse, France*

[b] *Laboratoire d'Hydrologie et de Géochimie de Strasbourg, Université de Strasbourg, EOST, CNRS, 67084 Strasbourg, France*

Received 10 May 2019; accepted in revised form 3 January 2020; Available online 11 January 2020

Abstract

Surface reactivity is a major parameter controlling mineral reactivity, and microscopic techniques investigating surface retreat with time have pointed at the heterogeneous and/or anisotropic reactivity of minerals, in relation with the diversity and stochastic distribution of energetic sites. However, in view of the discrepancies between rates determined in the laboratory, a thorough 3D approach of crystal reactivity might be particularly attractive to evaluate the respective contributions of single faces and crystal edges to the dissolution flux, and to fill the gap between the rates derived from face-specific, topography observations at micro-scale (i.e., with no contribution of the edges to dissolution) and those determined on crystal powders in continuously stirred reactors (with an overcontribution of the edges and surface defects to dissolution). Here, we provide a detailed 3D characterization of the geometry evolution and dissolution rate of a single crystal of calcite at pH 4.5 and 4.0 using X-ray micro-tomography (XMT) with a pixel size of 0.325 µm. Evaluation of the retreat and mapping of the reaction rates at the 3D crystal surface reveal a large range of dissolution rates reflecting the specific contributions of the different regions of the crystal. During dissolution and against all expectation, etch pits forming at the crystal surface progressively annihilate, primarily by intersecting with trains of steps coming from the near edge regions. The global rate determined at the crystal scale integrates the contribution of the local rates of all the crystal features, with $\bar{r}'_{corner} > \bar{r}'_{edge} > \bar{r}'_{cleavage} > \bar{r}'_{macrostep} \sim \bar{r}'_{pit} > \bar{r}'_{macrostep\ base}$. Crystal rounding reveals that contribution from the crystal edges progressively dominates the dissolution process over pit formation at the {10$\bar{1}$4} surfaces. The contribution of the edges to dissolution increases the crystal dissolution rate by at least 1.6 to what would be a face-specific dissolution, and will be size- and time-dependent, as suggested by a simple geometric model based on uniform or non-uniform dissolution of the faces of a model crystal. Finally, comparison of the method to vertical scanning interferometry measurements and scanning electron microscopy observations on surface portions shows that XMT imaging is robust, suggesting that its application to the dissolution/precipitation of other minerals would be highly beneficial to determine reliable rates that can be further used to model mineral reactivity.

© 2020 Elsevier Ltd. All rights reserved.

Keywords: Calcite dissolution; X-ray micro-tomography; 3D crystal geometry; Dissolution rate distribution; Surface topography; Rate mapping; Rate variability; Face-specific dissolution; Edge contribution

1. INTRODUCTION

Mineral reactivity is fundamentally important in Earth sciences, as it controls many of the natural or

* Corresponding author.
E-mail address: catherine.noiriel@univ-tlse3.fr (C. Noiriel).

https://doi.org/10.1016/j.gca.2020.01.003
0016-7037/© 2020 Elsevier Ltd. All rights reserved.

anthropogenic geochemical processes, such as continental weathering, diagenesis, hydrothermal alteration, carbon dioxide sequestration, nuclear waste disposal, groundwater contamination, or geothermal energy production (DePaolo and Orr, 2008; Kump et al., 2000; Morse and Arvidson, 2002; Noiriel and Daval, 2017; Steefel et al., 2005). In this regard, a specific attention has been paid over a century to the determination of reliable kinetic rate laws, with the ultimate goal to better understand, quantify and predict chemical transformations and mass transfer over large space and time scales. However, bridging the gap between rates measured in the field and determined in the laboratory remains an elusive objective, when already discrepancies exceeding largely the analytical errors have long been reported between reaction rates determined in the laboratory, despite the well-controlled physico-chemical conditions of the experiments (Fischer et al., 2014). All extrinsic factors being equal, this aspect points towards an intrinsic variability of mineral reactivity, which must be characterized and understood to ultimately upscale laboratory-derived rates to natural settings.

Intrinsic sources of variation have been highlighted through the measure of the distribution of local rates at the crystal surface (Fischer et al., 2012), which can be treated in the framework of the so-called "rate spectra" concept, and reflect the heterogeneous distribution of defects outcropping at the crystal surface. Therefore, it is not surprising that bulk dissolution rate data obtained from reactor experiments on crushed crystals (i.e., mineral powders) differs from dissolution rate data measured locally at the surface of polished or pristine crystals, due to differences in surface reactivity distribution at the two scales of observation, and also because sample preparation may play a key role in the resulting distribution of reactive sites. Surface reactivity, which is ultimately dependent on three parameters, i.e., chemical composition, atomic structure and fine-scale morphology (Hochella, 1990), can exert a crystallographic or microstructural control of mineral reactivity (Daval et al., 2013; Pollet-Villard et al., 2016a; Saldi et al., 2017). In this regard, microscopic techniques measuring the topography at the fluid-mineral interface are particularly attractive to investigate mineral reactivity.

Changes at the mineral surface can be evaluated *in situ* or *ex situ* by measuring the vertical retreat under various experimental conditions with micrometer to nanometer resolutions using methods such as atomic force microscopy (AFM) (Emmanuel, 2014; Hillner et al., 1992; Jordan and Rammensee, 1998; Shiraki et al., 2000; Stipp et al., 1994), vertical scanning interferometry (VSI) (Fischer and Luttge, 2007; Smith et al., 2013), phase shifting interferometry (PSI) (Ueta et al., 2013), confocal profilometry (Godinho et al., 2012), X-ray reflectivity (Fenter et al., 2000), digital holographic microscopy (DHM) (Brand et al., 2017) or X-ray microscopy (Laanait et al., 2015). Such methods have enabled measurements of dissolution rates on face-oriented single crystals or polycrystalline aggregates, and evidenced their variability at the mineral surface, with heterogeneous and/or anisotropic reactivity reflecting the energetic diversity of reactive sites. For instance, application of these techniques to the study of cleaved $\{10\bar{1}4\}$ surface of calcite has provided insightful observations of the contribution of etch pits and step retreat, or their interactions, to dissolution under a large variety of experimental conditions (Arvidson et al., 2006; Arvidson et al., 2003; Hillner et al., 1992; Shiraki et al., 2000; Smith et al., 2013 Bouissonnié et al., 2018; Duckworth and Martin, 2004; Jordan and Rammensee, 1998; Miyata et al., 2017; Ruiz-Agudo et al., 2009; Teng, 2004; Xu et al., 2010). Fine-scale observations at the crystal surface have also contributed to challenge the conventional treatment of reaction kinetics from mineral powders that has prevailed so far, which relies on the paradigms of homogeneity, isotropy and immutability (Noiriel and Daval, 2017) and on the definition of a unique reaction rate (Fischer et al., 2012).

However, these methods are often restricted to small observation surfaces (typically areas of less than $500 \times 500\ \mu m^2$). In addition, they often require the surface to be well cleaved or polished to provide surfaces as flat as possible, inherent to a limited vertical range (e.g., about 5 μm for AFM, and up to 150 μm for VSI). Consequently, they are often restricted to areas of lower reactivity (Dove and Platt, 1996) and ignore the contribution of surface macro-patterns and crystal edges. It has been pointed out that the missing contribution of the crystal edges and corners to the calculation of reaction rates could explain lower rates obtained from VSI measurements compare to bulk rate determination (Lüttge et al., 2003; Saldi et al., 2017). Although it has long been assumed that crystal edges provide a source of reactive sites (Schott et al., 1989), it is only very recently than the quantitative contribution of crystal edges to dissolution rates has been evaluated experimentally (Noiriel et al., 2019), using X-ray micro-tomography imaging (XMT). By enabling true 3D space, XMT should permit a significant extension to current methods and models by singling out the reactivity of crystal corners and edges, and to fill the gap between fine-scale (nm- to μm-scale) measurements of surface reactivity and macroscopic determination of bulk rates on powders.

In this study, we have quantified the dissolution rate of a whole crystal of calcite at pH 4.0 and 4.5 by providing a direct measurement of the retreat rates at the crystal surface using 3D XMT. We illustrate the heterogeneous distribution of the dissolution fluxes of the reacted crystal through time from almost 7.5 million data points analyzed at the crystal surface. The objective is to track the whole crystal topography at different time intervals in order to evaluate the contribution of the different surface and crystal features to the reaction rate distribution. In particular, we have evaluated the specific contributions of the crystal faces and edges on the long term, i.e., for an average surface retreat of 22.4 μm. The robustness of the method is discussed by comparing the crystal volume changes to chemical analyses of the calcium released during dissolution, and the 3D imaging of the crystal surface to vertical scanning interferometry and scanning electron microscopy (SEM) observations. As will be shown, the crystal edges play a major role in the dissolution process, which is quantitatively assessed. The average rates, which are in between the range of values reported for studies measuring the

surface topography and those derived from experiments on mineral powders can be considered as more representative for dissolution of calcite cements (i.e., sub-mm crystals) in nature.

2. MATERIAL AND METHODS

2.1. Sample preparation

A single calcite crystal about 1.8 mm long and 0.6 mm wide was obtained after crushing and sieving a cm-sized single spar crystal. The crystal was mounted on a glass capillary tube (Hilgenberg, 400 µm O.D.) using epoxy resin, which covers the bottom face of the crystal creating a mask that preserves it from dissolution. The crystal faces were not polished before the experiment, so that the different faces are not perfectly cleaved and they exhibit various macro-features such as ragged or curved cleavage macrosteps, hillocks, or rippled surface patterns, which are inherited from the breaking and size reduction of the original calcite sample (see further in Fig. 3). In particular, three of the four side faces (further named face 1, 2, and 4) exhibit well cleaved portions of surface along the $\{10\bar{1}4\}$ planes. Surface defects and macrosteps intersecting the aforementioned planes are visible, as well as, for face 1, macrosteps oriented along $\{01\bar{1}8\}$ parting planes. In contrast, the fourth side face (further named face 3) has a 5° miscut angle with respect to the $\{10\bar{1}4\}$ plane, and is dominated by macrosteps and rippled surface patterns. The top part of the crystal (further named face 5) is highly rough and stepped with many $\{10\bar{1}4\}$ plane intersects. Some defects of limited extension such as micro-fractures and cleavages are also noticed inside the crystal, as a few micro-particles at the crystal surface.

2.2. Dissolution experiment

The crystal was reacted at three time steps (t_1 to t_3) during 22.1 h with acidic solutions (pH 4.5 or pH 4.0) in a mixed-flow reactor (V=160 mL) at room temperature (25 ± 2 °C) and atmospheric pressure. The inlet solution was prepared with deionized water (18.2 MΩ cm^{-1}) + 0.01 M NaCl and the pH was adjusted to either 4.5 ± 0.1 or 4.0 ± 0.1 using analytical grade HCl. The flow rate Q was set to 8 cm^3 h^{-1} during the experiment using a Chemyx fusion syringe pump to maintain far-from-equilibrium conditions, and the solution was stirred at a rate of 400 rpm. The outlet fluid was collected continuously for analysis of the calcium released with Inductive Coupled Plasma - Mass Spectroscopy (ICP-MS 7500ce, Agilent Technologies). Internal spikes (In-Re), blank and calibration standards were used and replicate analyses were performed to assure accuracy and precision of the chemical analyses. However, because of the low concentration of Ca at the outlet (~10^{-6} M) and because the inlet solution contains some Ca as trace impurities in NaCl, it limits the accuracy of the mass balance evaluation.

The high fluid-to-mineral volume ratio allows for only a slight increase in the Ca concentration in the reactor, from $2.0 \cdot 10^{-6}$ to $6.0 \cdot 10^{-6}$ M, corresponding to a saturation state with respect to calcite of $\Omega < 10^{-9}$ throughout the experiment (calculated with Phreeqc v3.0 using the Phreeqc database, Parkhurst and Appelo, 2013). The experimental conditions are summarized in Table 1.

The reaction extent can be evaluated through the calcite amount removed from the crystal during the dissolution experiments. The amount of calcite dissolved at any time, $\Delta n_{calcite-chem}$ (mol), is given by:

$$\Delta n_{calcite-chem}(t_i) = \int_{t_0}^{t_i} \frac{\delta n_{calcite}}{\delta t}\delta t = \int_{t_0}^{t_i} F_{Ca}\delta t = \int_{t_0}^{t_i} Q \times \delta(\Delta\mathrm{Ca})\delta t = \sum_j V_j(\Delta\mathrm{Ca})_j \quad (1)$$

where $\delta n_{calcite}$ is the change in the amount of calcite (mol), F_{Ca} is the flux of calcium at the reactor outlet (mol s^{-1}), and ΔCa represents the difference between the outlet and inlet calcium concentrations, i.e., $[Ca]_{out}$ - $[Ca]_{in}$ (mol m^{-3}), j is the number of aqueous samples collected between t_0 and t_i and V is their volume (m^3).

2.3. 3D imaging with X-ray micro-tomography

The crystal was imaged before the reaction (t_0) and at the three time steps (t_1 to t_3) over the course of the dissolution experiment using 3D X-ray micro-tomography at the TOMCAT beamline (Stampanoni et al., 2006), Swiss Light Source (Paul Scherer Institute, Switzerland). The crystal was removed from the reactor for imaging in order to avoid any influence of the beam on the experiment (e.g., water radiolysis (Bras and Stanley, 2016; Laanait et al., 2015)). Indeed, in the range 5 < E < 40 keV, the photons do not possess enough energy to induce atomic displacements directly in crystalline materials (Bras and Stanley, 2016), so that the effects of radiation are non-significant.

A total of four data sets were collected during two different data acquisition sessions, with a pixel size of 0.325 µm, using a 10× magnification diffraction-limited microscope optics. Due to the large height of the crystal compared to the field of view of the sCMOS camera (pco.Edge 5.5, 2560 × 2160 pixels), three vertical scans were taken to image the whole crystal. Each data set is composed of 1701 radiographs collected over a 180° rotation range. Each radiograph was recorded with a monochromatic and parallel beam at the energy of 20 or 21 keV and an exposure time of 200 or 250 ms depending on the data acquisition session. Volume reconstruction was performed from the radiographs corrected from flat field and background noise using an algorithm based on the Fourier transform method (Marone and Stampanoni, 2012).

Image processing was achieved with Avizo® software. After reconstruction, the different sub-volumes at a given stage were stitched, resulting in volumes of about 1900 × 1250 × 5800 voxels. Note that due to the large displacement of the vertical stage and recalculation of the rotation axis during reconstruction, a slight mismatch at the junction between the different sub-volumes might be

Table 1
Summary of the experimental conditions.

Stage	Time (h)	Duration (h)	pH	Flow rate Q ($cm^3\ h^{-1}$)	XMT imaging
t_0	0				×
t_1	8	8	4.5 ± 0.1	8	×
t_2	19.1	11	4.0 ± 0.1	8	×
t_3	22.1	3.1	4.5 ± 0.1	8	×

observed. Then, the 3D grayscale volumes were normalized, converted to 8-bit integers, and denoised with a 3D median filter. The crystals were subsequently registered in the same coordinate system using the mutual information-based image registration approach (Maes et al., 1997). The different target volumes were aligned with the reference volume (at t_0), using a tri-linear interpolation technique to recalculate the gray value of the target voxels in the new coordinate system (Gonzales and Woods, 1992). Registration efficiency was evaluated thanks to marks identifiable inside the crystal, like micro-defects or micro-cracks.

2.3.1. Evaluation of the crystal volume and surface area

Evaluation of the crystal volume was performed following two different ways. The first method is based on the grayscale histograms of the XMT data sets. The three peaks for air, calcite and glass capillary are clearly identifiable on the histograms (Fig. 1), so that a simple threshold value half-way between the peak for air and the peak for calcite is chosen, after removal of the glass capillary peak. The calcite peak area represents the number of calcite voxels, and changes in the peak area of calcite are directly linked to the amount of calcite removed by dissolution.

The second method is based on segmentation of the grayscale data sets to provide a discretized geometry of the crystal. However, due to the large size of the data sets (~14 Gb), the volumes were resampled by a factor of two in every direction and interpolated with a Lanczos window function (Meijering et al., 2001) to reduce the volume size by an eight-fold factor before segmentation. The voxel resolution of the resulting volumes is thus 0.65 µm. A region-growing algorithm (Pitas, 2000) was used to separate the whole images into two phases, i.e. air and solid, by selecting, based on their gray-level, a certain amount of voxels which belong with certainty to one of the phases, and incrementally assigning indeterminate voxels to either the solid or the air phase. Although the peaks for air and calcite are well separated on the histograms, this technique is preferred over a simple thresholding method in order to remove the star artifacts present in the air phase, especially at t_0. Indeed, the star artifacts are very common at the intersection points of angulated elements such as the crystal, pits or macro-steps edges, and they can be confused with solid as they are very bright. After segmentation, the solid objects, i.e., crystal and capillary glass, and the artifacts were labeled in order to separate and remove the capillary glass and the artifacts from the images. The resulting volumes contain only the crystal.

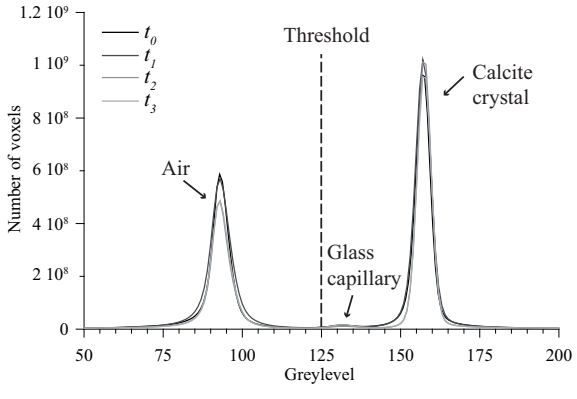

Fig. 1. Normalized histograms for the different XMT grayscale data sets. The differences in the peak areas for calcite and air both show the amount of calcite removed by dissolution (i.e., a decrease of the peak area of calcite and, as a result, an increase of the peak area of air).

The crystal volume $V_{crystal}$ (μm^3) is calculated at t_i from the number of element solid voxels n_{sol}, i.e., $V_{crystal} = n_{sol} \times V_{voxel}$, with V_{voxel} the volume of a voxel ($0.65 \times 0.65 \times 0.65\ \mu m^3$). The amount of calcite removed, $\Delta n_{calcite-XMT}$, can be evaluated at any stage of dissolution from the XMT volumes according to:

$$\Delta n_{calcite-XMT}(t_i) = \int_{t_0}^{t_i} \frac{\delta V_{crystal}}{\upsilon_{calcite} \times \delta t} \delta t = \frac{V_{crystal}(t_i) - V_{crystal}(t_0)}{\upsilon_{cal}} \quad (2)$$

where υ_{cal} is the molar volume of calcite ($m^3\ mol^{-1}$).

The crystal surface area (μm^2) is calculated at t_i from the number of solid-air pixel interfaces ($n_{sol-air}$), i.e., $S_{crystal} = n_{sol-air} \times S_{pixel}$, with S_{pixel} the surface area of a pixel ($0.65 \times 0.65\ \mu m^2$), which is the smallest element of surface area at the fluid-crystal interface. Note that the whole crystal was considered in the calculations, the surface area of the unreacted part of the crystal representing only about 0.05 % of the surface area of the crystal.

2.3.2. Examination of surface topography evolution

Surface topography evolution was evaluated locally on some small portions of the crystal faces. A few volumes of interest (VOIs) were extracted on faces 1, 2, and 3, from the grayscale data sets, with the voxel size of 0.325 µm. The mean planes of the crystal surface extracts were determined at t_0 and registered in a horizontal plane. The transformation was applied to the other VOIs, so that the topography evolution of the surface extracts is directly comparable. This technique is preferred over the extraction of the VOIs

from the segmented images, the direct registration of which, in a horizontal plane, would highlight interpolation steps at the crystal surface, which can be confused with crystal surface steps (see for instance Fig. 2 shown in Noiriel et al., 2019). After segmentation of the grayscale VOIs using the same procedure as described above (see Section 2.3.1), the topography of the fluid-solid interface was extracted. When the surface displays some overlaps (as it is the case, for instance, when micro-cracks are visible inside the crystal), the interface with the lowest surface elevation is selected.

2.3.3. Crystal dissolution rate

The global crystal dissolution rate r_{diss} (mol s^{-1}) and rate normalized to the surface area of the crystal $r_{diss-norm}$ (mol m^{-2} s^{-1}) were calculated after segmentation of the XMT data sets according to the following equations, respectively:

$$r_{diss} = \frac{\Delta V_{crystal}}{\upsilon_{cal}\ \Delta t} \tag{3}$$

and

$$r_{diss-norm} = \frac{\Delta V_{crystal}}{\overline{S_{crystal}}\,\upsilon_{cal}\ \Delta t} \tag{4}$$

with Δt a time interval (s), and $\Delta V_{crystal}$ and $\overline{S_{crystal}}$ the change in crystal volume (m^3) and the average crystal surface area (m^2) between two stages of dissolution, respectively.

2.3.4. Measure and mapping of the local dissolution rate at the crystal surface

Following the methodology described in Noiriel et al., 2019, the local dissolution rate r'_{diss} (μm h^{-1}) can be determined at any element (i.e., fluid-crystal pixel interface) of the crystal surface by analysis of the surface retreat after each dissolution stage. In their study, the surface retreat was calculated normal to the closest $\{10\bar{1}4\}$ surface. In the present paper, however, we have adopted a slightly different method in order to calculate the surface retreat normal to any element of the crystal surface instead of the retreat normal to the $\{10\bar{1}4\}$ surface. This methodology is motivated by the fact that: (i) every dissolution stage at t_i (starting from t_1) is compared with the previous one (t_{i-1}), and accounts for the changes of crystal morphology at the edges and corners at any stage of dissolution, and (ii) the crystal has a morphology far more complex than a simple rhombohedron. The method permits to measure the dissolution rate at the crystal surface regardless the crystal geometry or orientation.

Practically, the 3D Euclidean distance map (Akmal Butt and Maragos, 1998; Russ, 2011) outside of the crystal was computed at any time t_i (for $i = 1$ to $i = 3$). Consequently, each voxel outside the crystal at a given time is labeled with the distance normal to its surface, starting from the position of the fluid-crystal interface. Combining the distance map at t_i with the position of the fluid-crystal interface at t_{i-1} gives the surface retreat normal to the surface of the crystal at the previous stage of experiment, as illustrated in Fig. 2. In this case, for instance, the surface retreat at the crystal edges (or corners) is the distance normal to the considered edge (or corner), not the shortest distance (i.e., the distance normal) to the closest $\{10\bar{1}4\}$ surface.

Then, the local dissolution rate normal to the crystal surface is calculated according to:

$$r'_{\text{diss}} = \frac{d\,\mathbf{I_{fc}} \cdot \mathbf{n}}{dt} \tag{5}$$

with $\mathbf{I_{fc}}$ the fluid-crystal position vector, and $\mathbf{n}$ the normal to the crystal surface; the product $\mathbf{I_{fc}} \cdot \mathbf{n}$ is the surface retreat, i.e., the distance normal to the surface. The rate is expressed as a retreat velocity at the surface (nm s^{-1} or μm h^{-1}), but can be averaged at the crystal scale and normalized to the surface area by (e.g., Arvidson et al., 2004):

$$\bar{r}'_{\text{diss - norm}} = \sum_{n_{sol-fluid}} \frac{1}{\upsilon_{cal} \times n_{sol-fluid}} \frac{d\mathbf{I_{fc}} \cdot \mathbf{n}}{dt} \tag{6}$$

with $n_{sol-fluid}$ the number of voxels at the fluid-solid interface. It is also possible to determine the rate of specific faces, edges or other crystal features by averaging the local dissolution rates from VOIs defined in these areas:

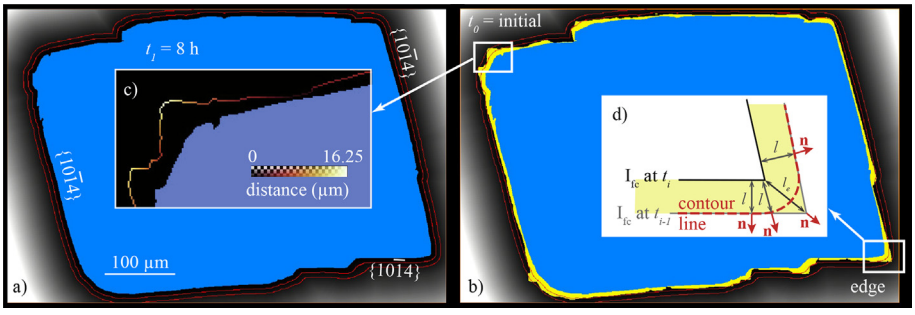

Fig. 2. Determination of the surface retreat between two stages of dissolution. (a) 3D distance map (grayscale) outside of the crystal (blue) at t_1 (shown in 2D cross-section), which represents the distance normal to the fluid-solid interface. Distance contours of 10 and 20 pixels (i.e., 6.5 and 13 μm) normal to the crystal surface are shown in red. (b) Combining the distance map with the crystal at t_0 (yellow) gives the retreat at the crystal surface between t_0 and t_1(inset (c)). Inset (d) highlights that, assuming a uniform dissolution of the crystal faces, the distance measured at the edge is actually the normal-distance to the edge, i.e. l_e, not the normal-distance to the surface $\{10\bar{1}4\}$ itself, i.e., l. $\mathbf{n}$ is the normal to the crystal surface at any point belonging to the fluid-crystal interface. (For interpretation of the references to colour in this figure legend, the reader is referred to the web version of this article.)

$$\bar{r}_k^{\,l} = \sum_j \frac{1}{j} \frac{d\mathbf{I}_{\mathbf{fc}} \cdot \mathbf{n}}{dt} \tag{7}$$

with k being a face, an edge, a corner or another crystal pattern, and j the number of fluid-solid interface pixels covering their surface. For the faces, VOIs of the same width (i.e, 150 pixels) were chosen in the central part of the flat portions of the faces (except for face 3) to limit as much as possible the contribution of edges to the determination of the rates. For the edges, VOIs of the same section, i.e. 150 × 150 pixels for the obtuse edges (i.e., edges 4-1 and 2-3, between face 4 and 1, and face 2 and 3, respectively; see Fig. 3 for location) and 125 × 150 pixels for the acute edges (i.e, edges 1-2 and 3-4) were defined at the same location for the different stages of the crystal evolution. As the crystal does not exhibit well identified corners, only one VOI around a large 5-4-1 corner (i.e., at the intersection between faces 5, 4 and 1, see Fig. 3 for location) was selected.

The local dissolution rates are computed between the two first experiment stages (i.e., between t_0 and t_1, and between t_1 and t_2) and can be directly mapped at the crystal surface, providing an overview of the dissolution rate distribution. The rates are provided in terms of surface retreat velocity, so that direct comparison is possible with data derived from AFM or VSI, provided that the retreat is also measured normal to the surface with these techniques. Appendix A gives further information about the measurement uncertainty, specifically inherent to the fluid-mineral positioning and registration issues. Since the number of fluid-crystal interface pixels decreases as dissolution progresses and the bin width of the histograms decreases with increasing dt, the dissolution rate distributions are normalized to the distribution at t_2 to allow for a better visualization.

2.4. Additional microscopic observations

In addition, characterization of the post-reacted sample was conducted using vertical scanning interferometry (VSI) and scanning electron microscopy (SEM) to provide a higher resolution characterization of the crystal surfaces. A Zygo New View 7300 VSI with a 50× Mirau objective allowed for mapping surface topographies with a spatial sampling of 0.219 µm along the x and y directions and an effective vertical resolution of 2–3 nm. The vertical scan range is however, limited to 150 µm, so that observations were restricted to quite flat surfaces. SEM observations were performed with a Jeol JSM-6360LV using the secondary electron mode. These measurements and observations at finer resolution are complementary and will be compared to XMT observations.

3. RESULTS

3.1. Evolution of the crystal morphology and surface topography

The initial crystal morphology, as described in Section 2.1, is shown in Fig. 3. Dissolution proceeds with heterogeneous face retreat at different scales.

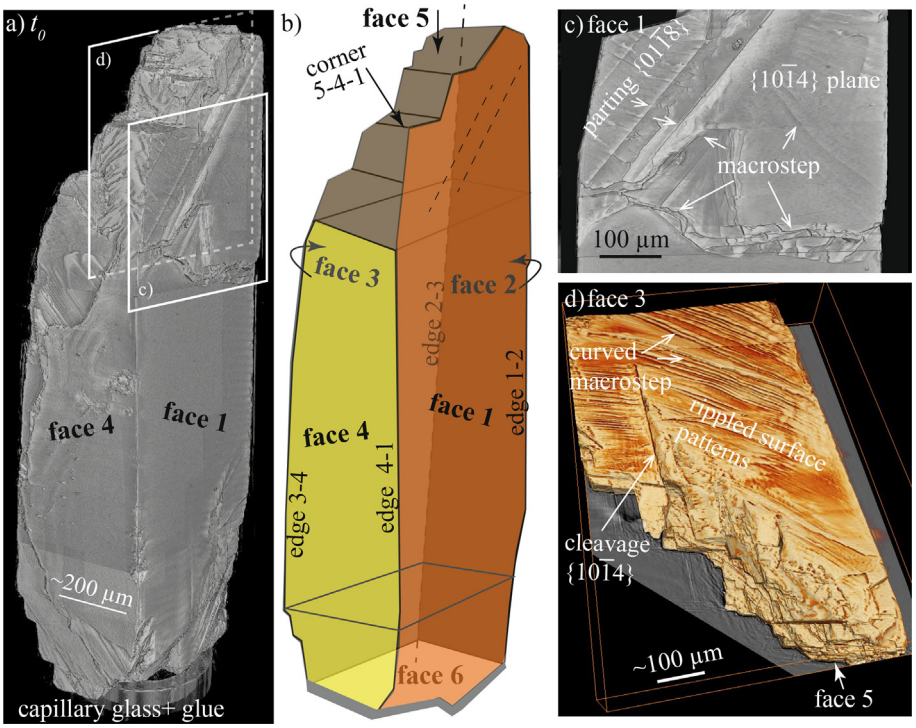

Fig. 3. (a) Volume rendering of the initial calcite crystal obtained from XMT and (b) schematic representation of the crystal morphology, with numbering of the different faces, edges, and corner. (c)–(d) Detailed surface patterns: (c) detail from face 1, showing a well cleaved {10 1 4} surface plane with macrosteps; the face is also intersected by several {01 1 8} parting planes, (d) detail from top part of face 3 covered by curved macrosteps and view of the rough crystal top showing many intersecting {10 1 4} planes.

At the crystal scale, dissolution of the surface macro asperities such as macro-steps, crystal edges and corners is faster than the average surface retreat (Fig. 4), due to the development of numerous steps over the crystal surface. As a result, the flat cleaved surfaces evolve progressively toward curved-shaped surfaces and the crystal becomes rounder with time (Fig. 4; see also topography profiles in Fig. 7). In contrast, dissolution rate in the topographic lows and at the base of the macro-steps is slower than in the surrounding areas (Fig. 4c).

At the face scale, the crystal topographies exhibit different evolutions depending on the initial face morphology. At t_1, the flat faces (i.e. portions of face 1, 2 and 4) are covered by sparse, macro etch pits (Fig. 5 and Fig. 6), whereas the step-like face (i.e., face 3) does not exhibit any etch pits (Fig. 8). The pits certainly result from merging of smaller pits that were formed at the surface at $t < 8$h, similarly to what has been observed in a comparable experiment at shorter times (Noiriel et al., 2019). The pits are about 90–160 μm in size and 4–7 μm in depth. Their density is variable depending on the face and location, about 100–130 per mm^2. Several etch pits are likely formed with the assistance of surface micro-defects, i.e., surface scratches, or micro-cracks that can be evidenced inside the crystal (Fig. 6a). Their geometry is complex (Fig. 6e), and they are generally deeper and remain longer visible than the others. With further reaction (i.e., at t_2 and t_3), the pits of the flat faces tend to annihilate, with a density decreasing to about 40 per mm^2. This observation confirms the trend in decreasing pit density with increasing dissolution observed in Noiriel et al., 2019. In fact, the development over the surface of numerous steps from the edges progressively annihilate the development of macro-pits, which vanish either by coalescence or by intersecting train of steps coming from the near edge region (Fig. 5b,c). Some pits whose dissolution rate becomes at some point slower than the surface average retreat are also evidenced (Fig. 5b,c). The anisotropy in step velocities between obtuse and acute steps developed parallel to the crystallographic directions $[\bar{4}\,41]$ and $[48\,\bar{1}]$, which results in asymmetrical pit formation, is also visible (Fig. 5b and Fig. 6b).

The evolution of face 3 with a 5° miscut angle is different from the cleaved faces. The surface, which contains a much higher density of steps, does not exhibit any etch pit formation (apart a few small ones along a cleavage continuity (Fig. 8)), but the initially curved macro-steps evolve to rippled or serrated steps with potentially rhombohedral endings near the edges (Fig. 9a).

In addition, dissolution is enhanced along straight asymmetric topographic lows corresponding to $\{10\,\bar{1}\,4\}$ cleavages (Fig. 5 and Fig. 8) or $\{01\,\bar{1}\,8\}$ parting planes (Fig. 9b) that were certainly created during crushing and size reduction of the original crystal. For example, the $\{10\,\bar{1}\,4\}$ cleavage identified at the bottom surface of face 1 reaches about 10 μm in depth from t_2 (Fig. 5c and Fig. 7a). Dissolution at cleavages is also anisotropic along the $[48\,\bar{1}]$ direction, similarly to what is observed at etch pits. Conversely, dissolution at parting planes does not

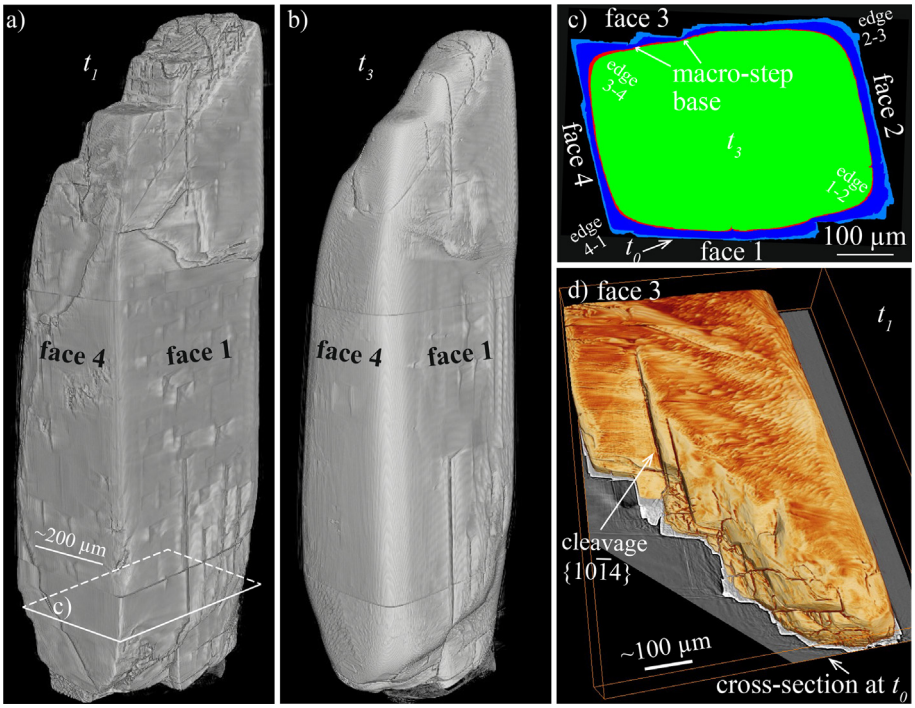

Fig. 4. Volume rendering of the calcite crystal obtained from XMT at time (a) t_1 and (b) t_3. (c) Cross-section of the superimposed segmented volumes from t_0 to t_3 showing heterogeneous surface retreat and rounding of the edges. The retreat between t_0 and t_1 is shown in light blue, between t_1 and t_2 in dark blue, and between t_2 and t_3 in red; the crystal at t_3 is in green. (d) Volume rendering of the top part of face 3 at t_1. (For interpretation of the references to colour in this figure legend, the reader is referred to the web version of this article.)

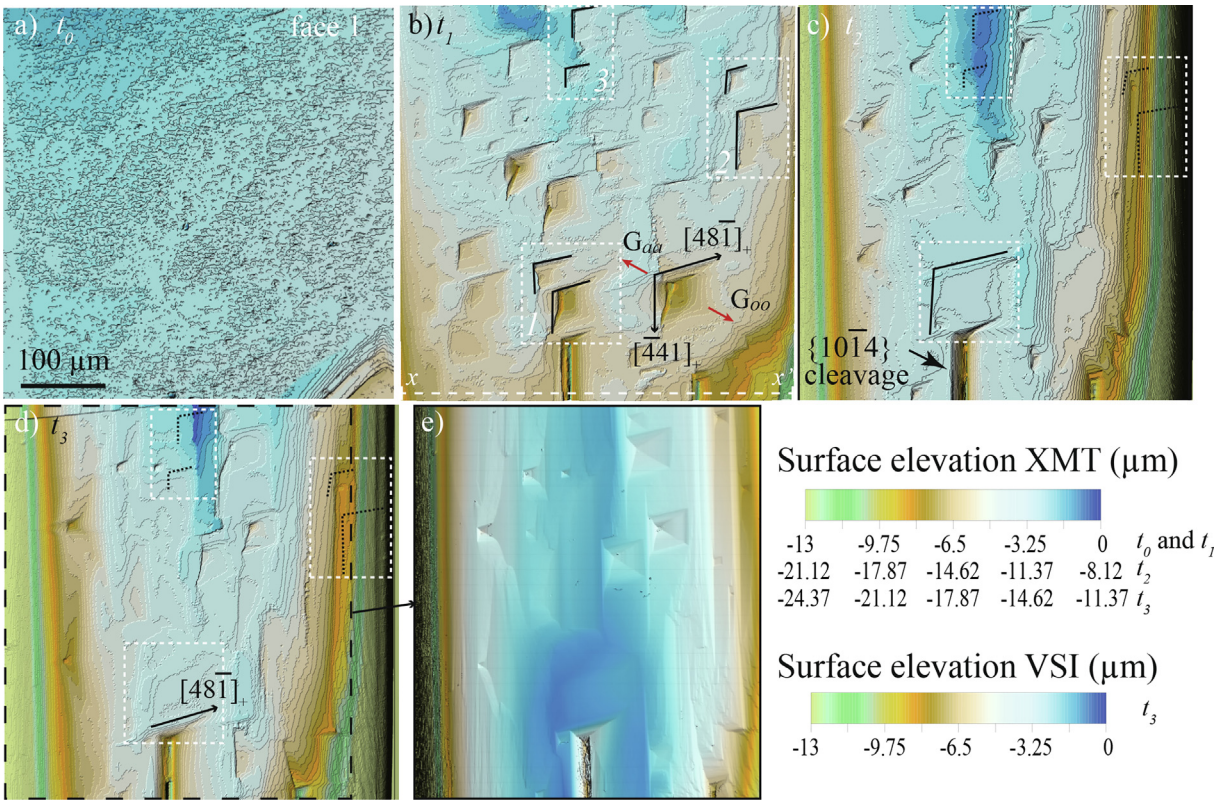

Fig. 5. Evolution of etch pit morphologies at the crystal surface. (a)–(d) XMT-derived topography for a surface extract of face 1 (455×455 µm^2), from t_0 to t_3. Note that the highest surface elevation at t_0 was set arbitrarily to 0, and that the range of elevations was shifted by 8.12 and 11.37 µm for t_2 and t_3, respectively. The figure shows pit annihilation by coalescence of two pits (inset 1), by intersection with a train of steps (inset 2) or by decrease of its rate of formation compared to the average surface retreat (inset 3). The black dotted lines correspond to the reported position of some etch pits at t_1. The white dotted xx' line in (b) denotes the position of the topographical profiles shown in Fig. 7a. (e) VSI-derived topography at t_3. Note that the image is not exactly superimposable with the corresponding XMT image and that the origin for vertical range is arbitrary.

appear anisotropic. Nevertheless, it generates macrosteps at the crystal surface, probably inherent to step propagation along these discontinuities (Fig. 9b).

Finally, the edges are covered with either macrosteps with long straight edges or highly kinked macrosteps with rhombohedral ending (Fig. 9a,c,d). Their morphology actually depends on the intersection between the calcite dissolution planes with the curved topography of the crystal (Fig. 8 and Fig. 9). The patterns have similarities with those observed at finer scale on misoriented polished surfaces (Bisschop et al., 2006; Smith et al., 2013). However, with further dissolution, it is worth noting that some flat surface portions reappear near the crystal edges (Fig. 9c,d and Fig. 5), often in the continuity of former etch pit propagation direction.

3.2. Global dissolution rate and surface rate distributions

The experimental calcite crystal dissolution takes place under far-from-equilibrium conditions, with the saturation state Ω ($\Omega = IAP/K_{s\ calcite}$) remaining below 10^{-9}. The amount of dissolved calcite derived from XMT and chemical balance is depicted in Fig. 10. First, the figure shows that the amount of calcite derived from the XMT processing techniques, i.e. the (i) grayscale histograms and (ii) segmented data sets, are in very good agreement. However, at t_2 and t_3, the results are slightly lower than $\Delta n_{calcite-chem}$ derived from chemical analyses.

Analysis of the XMT segmented data shows that both the crystal volume and surface area decrease during dissolution (Table 2). At the end of the experiment, 21.4% of the crystal was dissolved. The global dissolution rates, r_{diss}, as well as the average surface normalized rates, $r_{diss-norm}$, are also presented in Table 2. In this study, the global rate was normalized to the surface area determined at the scale of the XMT imaging technique. The specific surface area of the unreacted crystal determined this way is 43.9 cm^2 g^{-1}, which is 2.7 times smaller than the surface area determined by BET (Brunauer et al., 1938) on similar calcite crystals (120 cm^2 g^{-1}, Noiriel et al., 2012). As expected, the global rate is higher at pH 4.0 ($9.25 \cdot 10^{-6}$ mol m^{-2} s^{-1}) than at pH 4.5 ($5.46 \cdot 10^{-6} \pm 1.21 \cdot 10^{-6}$ mol m^{-2} s^{-1}). The rate determined at pH 4.0 is in good agreement with the data obtained by Noiriel et al., 2019 using the same technique and at the same pH value. The rate determined at pH 4.5 seems to increase with increasing

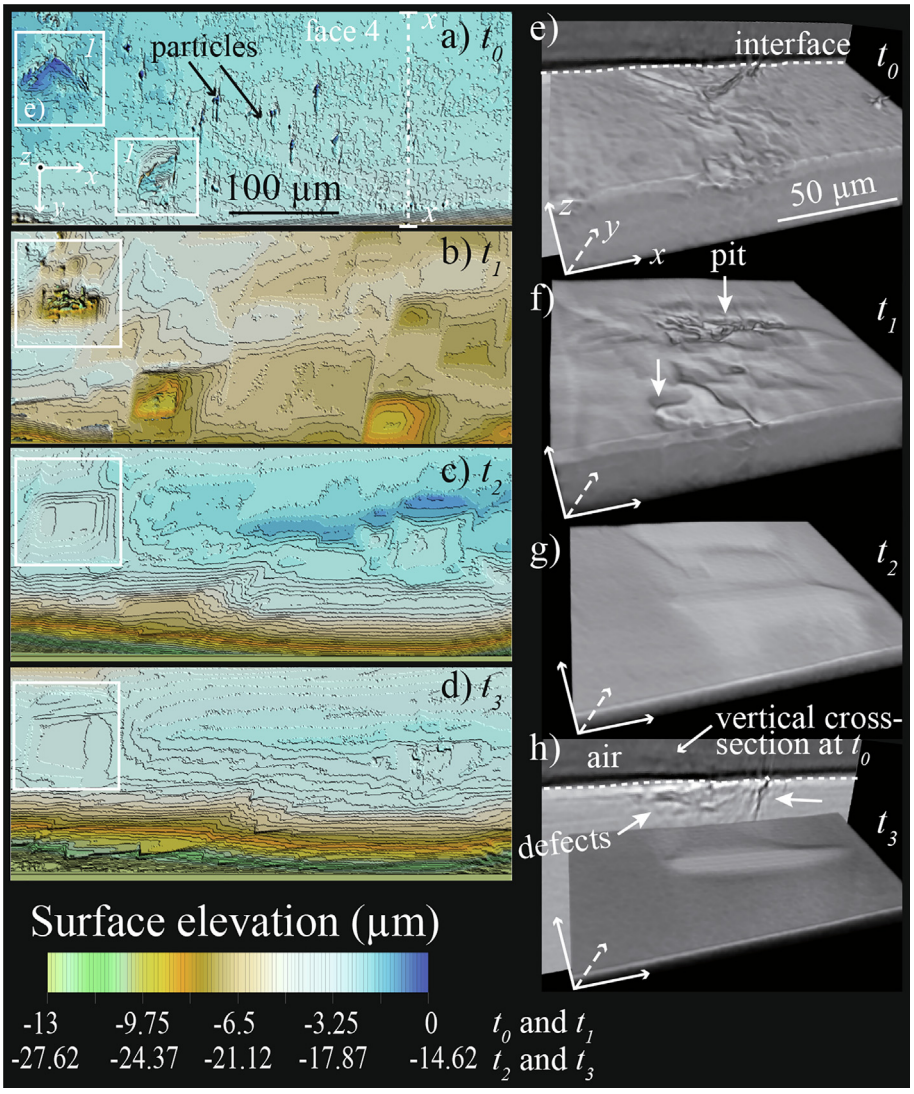

Fig. 6. Evolution of etch pit morphologies at the surface of face 4 (surface extract of 455 × 195 µm^2) (a)–(d) XMT-derived topography from t_0 to t_3. Note that the highest surface elevation at t_0 and t_1 was set arbitrarily to 0, and that the range of elevations was shifted by 14.62 µm for t_2 and t_3. (e)-(h) Details of the evolution of a pit geometry (3D rendering view) which initiated thanks to macro-defects that are visible at the surface (inset 1) and also inside the crystal. Note that the views are flipped vertically compared to the orientation in (a)–(d). The vertical white dotted *xx'* line in (a) denotes the position of the topographical profiles shown in Fig. 7b.

dissolution time, but it is difficult to decipher whether it results from the crystal geometry changes or from the preceding dissolution stage at pH 4.0 (i.e., between t_1 and t_2).

More interesting is the evaluation of the local dissolution rates directly mapped at the crystal surface (Fig. 11), as well as the derived rate distributions (Fig. 12). The local dissolution rates at the crystal surface reach on average 0.59 (between t_0 and t_1), 1.34 (between t_1 to t_2), and 0.94 µm h^{-1} (between t_2 to t_3) (Table 2). The average local normalized rates, $\bar{r}'_{diss-norm}$, differ slightly from the global rates, $r_{diss-norm}$, which are in turn normalized to the total crystal surface area (Table 2). Mapping of the dissolution rates confirms the observations made from the surface retreat. The average dissolution rate results from the contribution of the different crystal surface patterns to dissolution at very different rates. The reactivity extracted from small VOIs at the crystal corner ($\bar{r}'_{corner}$) and edges ($\bar{r}'_{edge}$) appears to be the fastest process, followed by the reactivity of the cleavage micro-fractures and parting planes ($\bar{r}'_{cleavage}$), macrosteps ($\bar{r}'_{macrostep}$) and etch pits ($\bar{r}'_{pit}$), faces, and finally topographic lows and base of macrosteps ($\bar{r}'_{macrostep\ base}$) (Fig. 11 and Fig. 12b,c).

4. DISCUSSION

4.1. Application of X-ray micro-tomography for tracking crystal reactivity

XMT is a noninvasive and nondestructive imaging technique relying on the 3D reconstruction of a sample from a series of 2D radiographic projections taken at about a

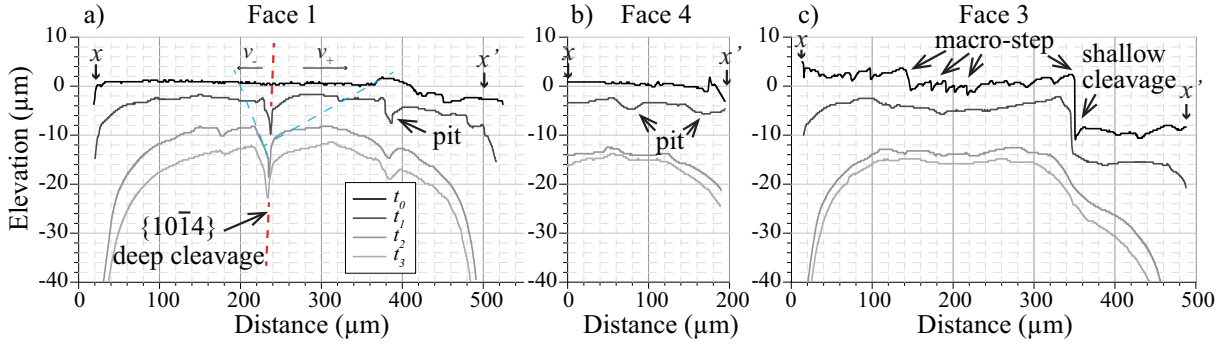

Fig. 7. Topography evolution (xx' profiles) of (a) face 1 (b) face 4 and (c) face 3 at the different times of the experiment (see Fig. 5, Fig. 6 and Fig. 8 for the localization of the profiles). The red dashed line underlines the direction of a {10$\bar{1}$4} cleavage. The blue dashed lines underline the direction of the $[48\,\bar{1}]_+$ and $[48\,\bar{1}]_-$ facets at t_2. (For interpretation of the references to colour in this figure legend, the reader is referred to the web version of this article.)

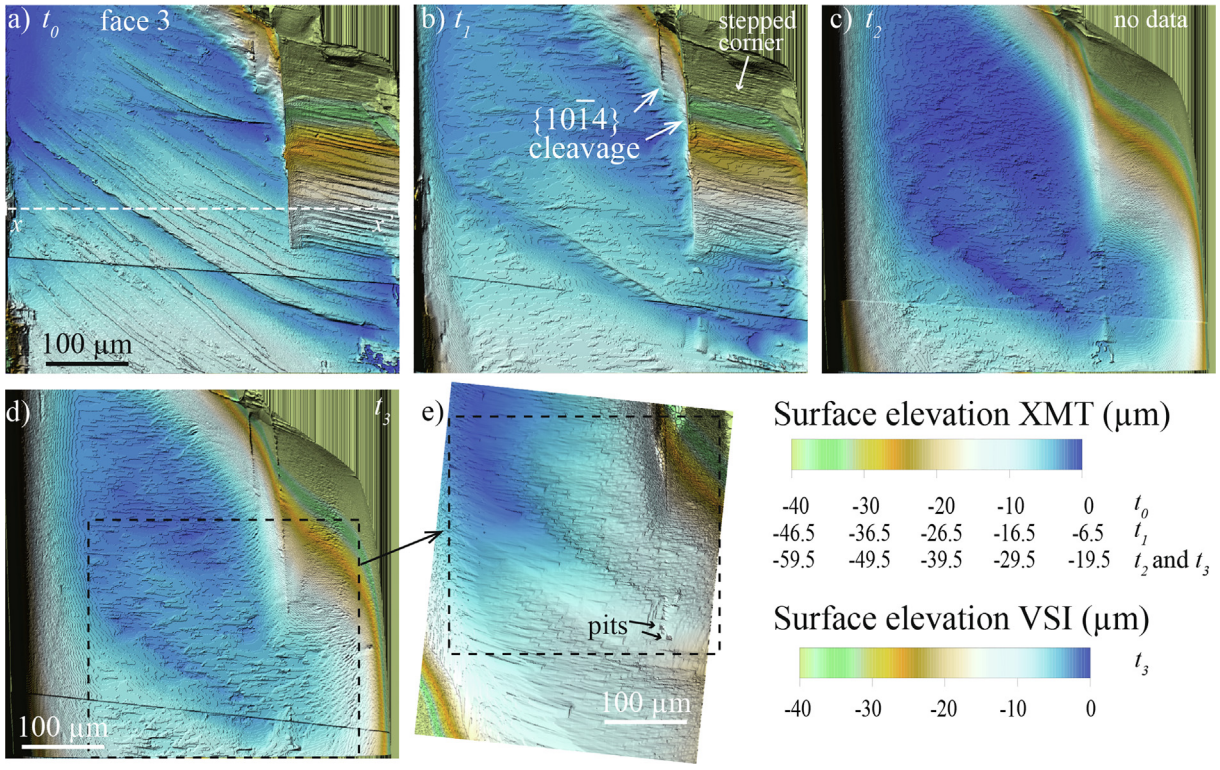

Fig. 8. Evolution of the surface morphology of face 3. (a)–(d) XMT-derived topography from t_0 to t_3 (surface extract of 487 × 487 µm^2). Note that the highest surface elevation at t_0 was set arbitrarily to 0, and that the range of elevations was shifted by 6.5 µm for t_1, and by 19.5 µm for t_2 and t_3. (e) VSI-derived topography at t_3. Note that the image is not superimposable with the corresponding XMT image and that the origin for vertical range is arbitrary. The horizontal dotted xx' line denotes the position of the topographical profiles shown in Fig. 7c.

thousand of different angular positions over 180°. The development of fast detection systems, high-quality optics, high data rate streaming and computational capabilities has resulted in new perspectives for the application of XMT imaging (Marone and Stampanoni, 2012; Villanova et al., 2017), such as *in situ* dynamic tracking of fast reactions with a micrometric resolution, or *ex situ* imaging with a submicrometric resolution (i.e., with a pixel size up to about 50 nm) at well-spaced time intervals, like in this study.

Admittedly, XMT has a lower resolution than VSI, especially in the direction perpendicular to the surface. For instance, XMT and VSI maps reported in Fig. 5d,e and Fig. 8d,e show that the finest details are not resolved, like the pit topography or some surface details. However, there is a high degree of consistency between the methods, and all the etch pits observed with VSI are identifiable with XMT. XMT reveals also a good match with SEM observations in areas where VSI is unable to capture the surface elevation due to steep topographical changes (Appendix B).

Comparison of VSI and XMT techniques for five different profiles at the surface of face 1 (Fig. A1 in Appendix A) shows that XMT effectively may misestimate the position of

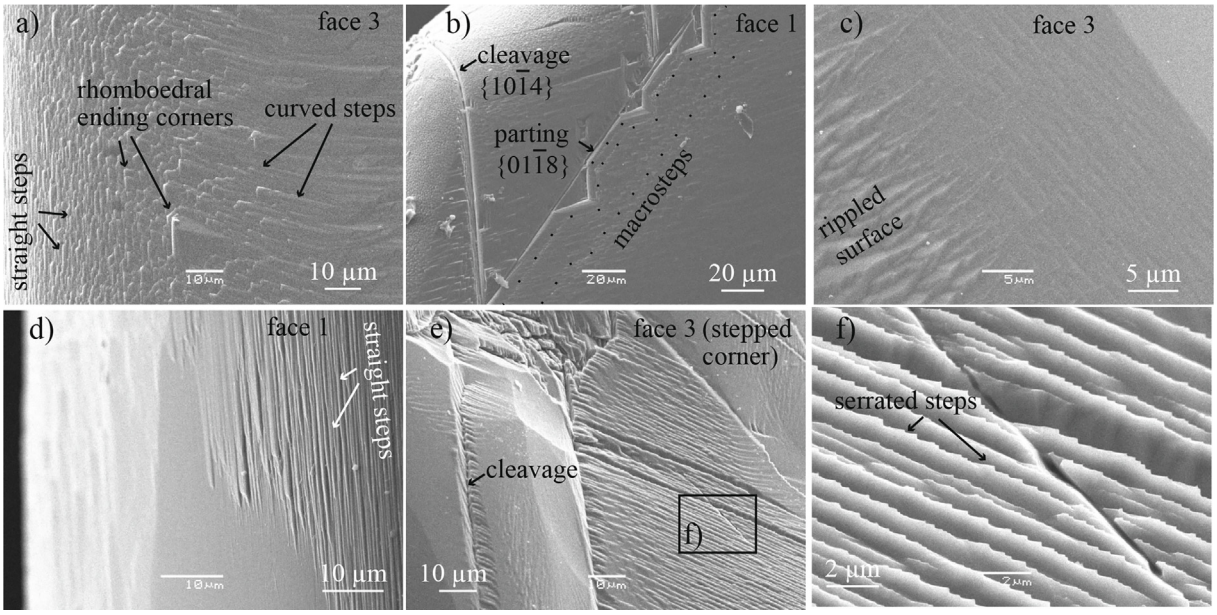

Fig. 9. SEM observations of the calcite crystal at t_3. (a) Rhombohedral ending corners at the junction between straight steps and curved steps at the crystal edge 2–3. (b) Anisotropic dissolution across a {10$\bar{1}$4} cleavage and dissolution across a {01$\bar{1}$8} parting plane intersecting several {10$\bar{1}$4} cleavages; the black dots underline macrosteps propagating at the crystal surface from the parting plane. (c) Transition between rippled steps and flat surface portion at the crystal edge 3–4. (d) Transition between straight steps and flat surface portion at the crystal edge 1–2. (e) Highly cleaved and fractured area near cleavages (stepped corner of face 3, see Fig. 8 for location) exhibiting (f) serrated steps.

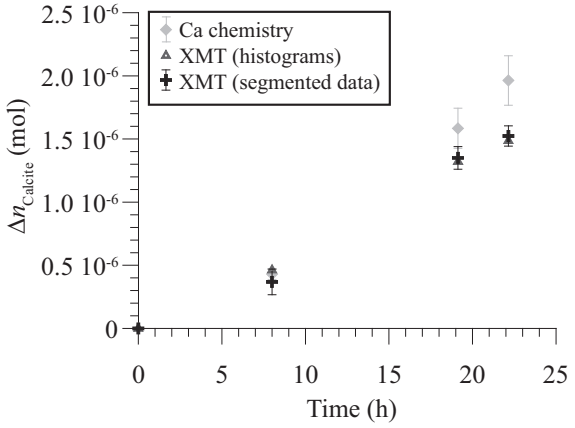

Fig. 10. Amount of calcite dissolved during the experiment, calculated from XMT grayscale or segmented data sets ($\Delta n_{calcite-XMT}$) and from Ca chemical balance ($\Delta n_{calcite-chem}$). The error bar on the data derived from XMT segmented data set is calculated assuming an error of ± 1 pixel (i.e., 0.65 µm) on the position of the fluid-crystal interface.

the fluid-mineral interface, especially at high elevations. An uncertainty estimate of ±1 pixel seems nonetheless reasonable when comparing the different profiles. The inability of XMT to capture some surface details does not arise only from the imaging resolution, and some inherent noise can also alter the images. Indeed, XMT does not provide a direct measurement of the surface topography. Conversely, the topography is extracted from the 3D reconstructed grayscale volumes of the crystal after segmentation. This makes the accuracy on the fluid-mineral positioning dependent on the grayscale image quality. In particular, the star artifacts, which are noticed over the crystal surface (especially in the data set at t_0), manifest themselves as bright or dark streaks where angular shapes exist, like at the crystal edges, in micro-cracks and etch pits. Consequently, they can introduce a bias locally on the topography extracted by altering image segmentation (see, for instance, the vertical depressed area around the particles in Fig. 6a). In particular, they were identified to be the cause of the topography alteration near the high elevation patterns.

Nevertheless, the technique has advantages over other surface-sensitive methods, as there is no restriction on the

Table 2
Summary of the experimental results obtained from XMT imaging and comparison with the rates obtained from chemistry.

Stage	Time (h)	pH	Crystal volume (m^3)	% dissolved	Crystal surface area (m^2)	r_{diss} (mol s^{-1})	$r_{diss\text{-}norm}$ (mol m^{-2} s^{-1})	$\bar{r}'_{diss}$ (µm h^{-1})	$\bar{r}'_{diss-norm}$ (mol m^{-2} s^{-1})	$r_{diss-chem}$ (mol s^{-1})
t_0	0		$2.63 \cdot 10^{-10}$	0	$3.12 \cdot 10^{-6}$					
t_1	8	4.5	$2.49 \cdot 10^{-10}$	5.3	$2.89 \cdot 10^{-6}$	$1.28 \cdot 10^{-11}$	$4.26 \cdot 10^{-6}$	0.59	$4.43 \cdot 10^{-6}$	$1.50 \cdot 10^{-11}$
t_2	19.1	4.0	$2.13 \cdot 10^{-10}$	19.0	$2.43 \cdot 10^{-6}$	$2.46 \cdot 10^{-11}$	$9.25 \cdot 10^{-6}$	1.34	$1.01 \cdot 10^{-5}$	$2.88 \cdot 10^{-11}$
t_3	22.1	4.5	$2.07 \cdot 10^{-10}$	21.3	$2.39 \cdot 10^{-6}$	$1.61 \cdot 10^{-11}$	$6.67 \cdot 10^{-6}$	0.94	$7.11 \cdot 10^{-6}$	$3.48 \cdot 10^{-11}$

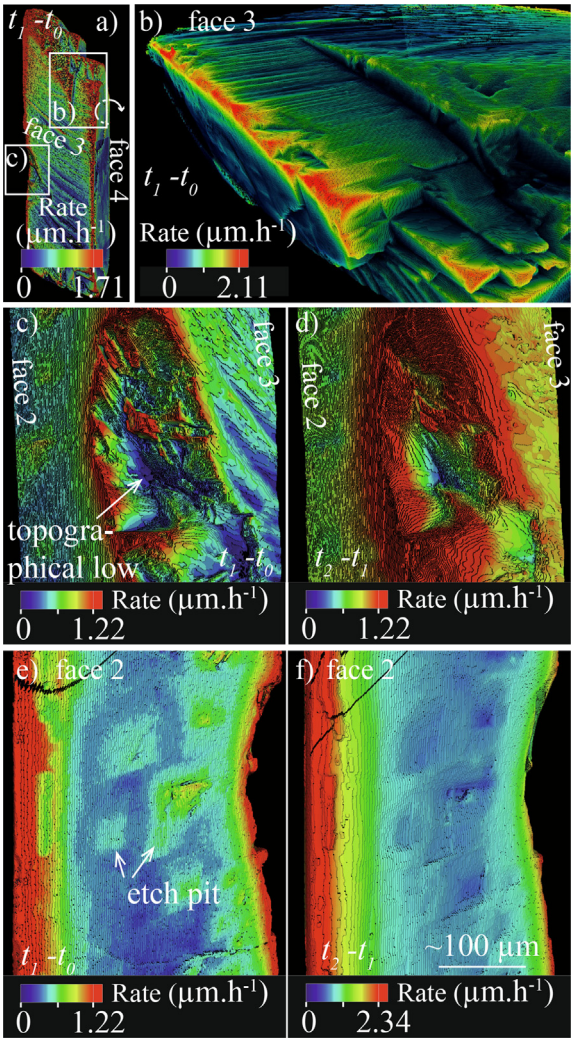

Fig. 11. Mapping of the local dissolution rate $\bar{r}'_{diss}$ (µm·h^{-1}) at the crystal surface. (a) Mapping of the whole crystal between t_0 and t_1, showing higher rates at the crystal edges and corners. (b) Detail of the stepped corner in face 3. (c)-(d) Detail of the topographic low at the edge 2–3 at (c) pH 4.5 (i.e., between t_0 and t_1) and (d) pH 4.0 (i.e., between t_1 and t_2). (e)-(f) Detail of the local rates at the surface of face 2 at (e) pH 4.5 (i.e., between t_0 and t_1) and (f) pH 4.0 (i.e., between t_1 and t_2). Note that values in red exceed the maximum values indicated in the scale bars.

crystal orientation or geometry, especially in terms of face orientation or surface roughness, so that any type of crystal or surface morphology can be analyzed. No specific preparation that can affect mineral reactivity (e.g., polishing or crushing) is required, and the whole crystal geometry is provided, accounting for the reactivity of all the faces, edges and corners. In addition, experiments are not restricted to small surface retreat due to unlimited vertical range, so that exploration of reactivity on the long term is possible. The technique also allows for recalculating the changes in the geometric surface area with time, something useful for the conventional rate normalization. Finally, XMT can provide extra information about defects that are located below the surface, i.e., inside the crystal, such as micro-cracks, cleavages, fluid or mineral inclusions, which can contribute at some point to the reactivity, but are hidden from the view of other techniques measuring the topography.

Then, the reliability of the method to provide accurate rate distributions from experiments performed *ex situ* relies on the ability to perfectly reference the sample in the same coordinate system, as the crystal has to be moved in and out of the beamline between acquisitions and dissolution experiments. In this case, registration problems can also affect the accuracy of the surface retreat determination (Fig. A2 in Appendix A). In the present study, for instance, clipping of the crystal in three sub-volumes which exhibit a small mismatch and rotation axis tilt did not make registration of the crystal perfectly accurate. When the retreat is too small compared to the pixel size (e.g., between t_2 and t_3), it increases the relative error on the retreat determination. However, this problem of registration could be easily overcome in the future by limiting imaging of the whole crystal to one data set, thus decreasing the pixel size for the crystal to fit in the field of view of the camera, or by creating some masked areas at the crystal surface to facilitate 3D registration of the different data sets.

4.2. Contribution of the crystal edges and corners

Dissolution at edges and corners increases the population of step and kink sites over time (Arvidson et al., 2003; Briese et al., 2017; Chen et al., 2014; Lüttge et al., 2013), consistently with larger dissolution rates measured at the crystal edges and corners. During dissolution of calcite at pH 4.0, Noiriel et al., 2019 estimated the dissolution rate of the crystal edges to be 1.7 times higher than the faces. The result is consistent with this study, where the rate was found to be 2.0 (pH 4.5) and 2.1 times (pH 4.0) higher in average at the crystal edges (Fig. 12b,c). The only difficulty in quantifying the contribution of the crystal edges is that their limits become undefined from t_0, i.e. from the time that the sharp edges evolve to rounded ones, so that the rate distribution at the edges depends on their extension in the VOIs used for calculation.

Although the edge regions are likely to be dominated by macro-steps, i.e., merged steps formed by step bunching, step pinning and step-step interactions (Bonzel, 2003; Smith et al., 2013), whose velocity is decreased compared to monolayer steps (Akutsu, 2014), it does not limit the lateral extension of the vicinal r-plane edge surfaces from the edges, as suggested by the rounded topographical profiles (Fig. 7). By extending the asymmetrical facets of the cleavage in the $[48\bar{1}]_+$ and $[48\bar{1}]_-$ directions up to the initial surface (red and blue dashed lines in Fig. 7a), we estimate obtuse (v_+) and acute (v_-) step velocities of 1.5 and 0.64 nm s^{-1} between t_0 and t_2 (Fig. 7a), two values lower but in reasonable agreement with the velocities obtained at pH 4.3 by De Giudici, 2002 (i.e., 4.3 and 1.1 nm s^{-1} for steps oriented along the two equivalent directions $[\bar{4}41]_+$ and $[48\bar{1}]_+$, and $[\bar{4}41]_-$ and $[48\bar{1}]_-$, respectively). These values are largely higher than the face-specific (i.e., normal to the surface) average retreat velocities of 0.1 (pH 4.5) and 0.24 nm s^{-1} (pH 4.0) (Fig. 12b,c), that could

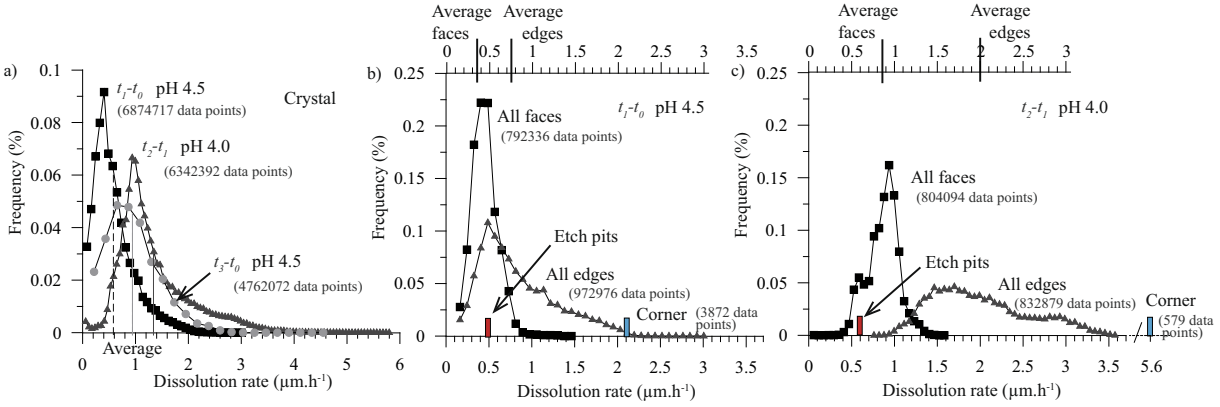

Fig. 12. (a) Local rate distribution at the surface of the whole crystal. The rates are normalized to the distribution at t_2 for the sake of visualization. (b)–(c) Averaged rates determined for the four faces and edges (extracted from 8 different VOIs), and for the corner (extracted from 1 VOI) at (b) pH 4.5 (i.e., between t_0 and t_1) and (c) pH 4.0 (i.e., between t_1 and t_2). The rates evaluated for the etch pits shown in Fig. 11e,d are also presented. The number of data points in the VOIs used for the calculation of the histograms is also indicated.

be assumed to result, in first approximation, of the layer-by-layer stripping during stepwave propagation. Compared to the average retreat velocities of 0.21 (pH 4.5) and 0.55 nm s^{-1} (pH 4.0) determined at the crystal edges, this also supports the assumption that the step density coming from the edges is higher than those coming from the flat surface. Consequently, contribution of the crystal edges to dissolution through the propagation of high velocity trains of steps overrides progressively the effects of the dissolution normal to the $\{10\bar{1}4\}$ faces through pit formation and growth (i.e., the face-specific dissolution).

This finding compares also well with a macroscopic comparison model between the experimental dissolution of the crystal (hereinafter referred to as the experiment) and a hypothetic, uniform dissolution of the crystal faces (hereinafter referred to as the uniform dissolution case). Uniform dissolution of 2.5% (from the crystal geometry at t_0) and 7.9% (from the crystal geometry at t_1) in volume of the crystal faces allows for the faces of the scaled crystal to fit in the faces of the real crystal at t_1 and t_2, respectively (Fig. 13a,b). Based on the volume ratios of the crystal in the experiment over the uniform case, accounting for the contribution of the edges shows that the dissolution rate in the experiment is roughly 2.1 time faster between t_0 and t_1, and 1.5 time faster between t_1 and t_2 compared to what would be a face-specific contribution in the uniform dissolution case. Overall, between t_0 and t_2, the dissolution rate is 1.6 time higher in the experiment compared to the uniform dissolution case. These results are consistent with the edge-to-surface retreat ratios, as defined by: l_a/l and l_o/l for acute or obtuse edges (with l the retreat normal the face surface, and l_a and l_o the retreat normal to the acute and obtuse edges, respectively). The ratios l_a/l and l_o/l are equal to 1.59 and 1.28, respectively, for a uniform dissolution of a parallelogram, as illustrated in Fig. 13d. Calculating the ratios from the XMT data show that the dissolution along the edge bisectors is overall 2.4 time faster in the experiment compared to the uniform dissolution case. Rounding of the crystal edges is thought to decrease the edge to surface retreat ratio with increasing dissolution, although it is still visible at t_3 (pH 4.5) that the edges have a higher surface retreat than the faces (Fig. 4c).

Finally, it is also possible that the crystal edges experience a higher diffusive flux at their surface in relationship with local hydrodynamic conditions, as dissolution of calcite is diffusion-limited far from equilibrium under acidic pH (Plummer et al., 1978; Rickard and Sjöberg, 1983), with the result of enhancing their progressive control to crystal dissolution. Nevertheless, Saldi et al., 2017 suggested that the reactivity of edges and corners is not limited to low pH and far-from-equilibrium conditions, and should also be considered carefully at basic pH and near equilibrium conditions, as the edges can also be the main source of steps moving while etch pit nucleation at point defects and dislocation would be comparatively unfavorable in these conditions.

4.3. Size- and time-dependent reactivity model

The rate data determined in this study are characteristic of the present crystal (i.e., with a given size and aspect ratio), but, all in all, these observations point out that the edge to face-specific contribution will be size-dependent. To the first order, the respective contribution of edges and faces to crystal dissolution can be modeled using simple geometric considerations that are detailed in Appendix C. To emphasize the role of the crystal edges, an ideal case of uniform dissolution of the faces, similar to the actual sketch represented in Fig. 13d was compared to a dissolution case including extra contribution of the edges to the dissolution flux (hereinafter referred to as the non-uniform dissolution case). The contribution of the edges to the dissolution flux was approximated to that of the development of facets with an orientation normal to the bisectors of the four angles that define an ideal parallelogram. Importantly, our approach is not mechanistic but

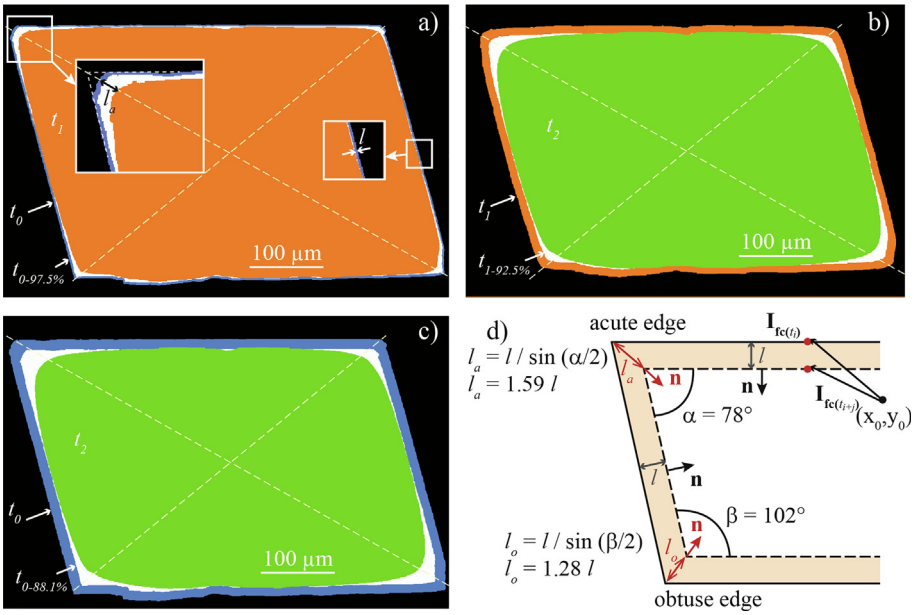

Fig. 13. Superimposed cross-sections of the crystal (a) at t_0 (blue) and t_1 (orange), (b) t_1 and t_2 (green), and (c) t_0 and t_2, and comparison with a hypothetic, uniform dissolution of the crystal faces of 2.5% (a), 9.7% (b) and 11.9% (c) in volume (white). Inset 1 shows that the edges are not necessarily sharp, even at t_0. The white area corresponds to the difference of volume of material removed between the experimental data and the model of uniform dissolution of the crystal faces (i.e., ignoring the edge contribution). (d) Sketch comparing the surface retreat normal to the {10$\bar{1}$4} faces (l) and at the acute (l_a) and obtuse (l_o) edges for a uniform dissolution of the crystal faces; **n** is the normal to the surface. (For interpretation of the references to colour in this figure legend, the reader is referred to the web version of this article.)

geometric; as a consequence, it provides a lower bound for the actual contribution of edges, since the lateral propagation of steps from the edges on the surface is ignored.

The evolution of the expected extent of reaction of a model crystal with dimensions similar to the one used in the present study (500 × 300 µm) with no extra contribution of the edges (uniform dissolution case) is compared to that of a crystal with preferential dissolution occurring at the edges (non-uniform dissolution case) (Fig. 14a, b). The rate parameters were derived from the dataset discussed in the previous section. As can be seen, the contribution of edges is responsible for a deviation from the sub-linear trend depicted by the trend observed for the uniform case (Fig. 14a). After 22.1 hours (corresponding to the duration of the experiment), the extent of reaction is 25% greater because of the contribution of edges, whose dissolution is roughly responsible for one third of the dissolution flux (Fig. 14b). This contribution is anticipated to become increasingly significant as the dissolution proceeds and the crystal shrinks.

As a consequence, an important concern is how these results obtained with a crystal having the dimensions of the one used in the present study translates to crystals with other grain sizes typical of those used in powder dissolution experiments. To address this question, sensitivity tests were performed and are depicted in Fig. 14c, which represents the evolution of the ratio of the non-uniform (i.e., where the reactivity of edges is considered to be similar to that measured in the present study) over uniform (i.e., where the reactivity of edges is dictated by the inwards progression of faces) calcite dissolution rate as a function of time. A ratio greater than 1 corresponds to a dissolution rate that is gradually driven by edges, whereas a value of 1 indicates that the contribution of edges is not significant, and that the classical normalization of the rates to the surface area may remains valid. As can be expected, the contribution of edges increases when the grain size decreases (Fig. 14c). Over durations as short as ~3 days, the enhanced dissolution at edges is responsible for doubling the dissolution flux for crystals with arbitrary dimensions of 50 × 30 µm. The time required to reach such a value is obviously much longer as the crystal size increases, and can be as high as ~2 months for crystals in the mm-size range. These results illustrate how sensitive is the dissolution of calcite crystals to the crystal size, an effect which must be taken into account when running powder dissolution experiments, and which is less significant for, for instance, VSI experiments conducted with cm-sized crystals. These results also challenge the proper definition of a unique and time-invariant "dissolution rate constant" for crystals, as previously emphasized by Pollet-Villard et al., 2016a or Briese et al., 2017, with similar arguments.

4.4. Contribution of the misoriented face and crystal defects

In this study, it is difficult to evaluate precisely the contribution of the misoriented face (i.e., face 3) due to registration issues, although it seems that the dissolution rate is higher for face 3 than for face 1 and that the discrepancy is even more pronounced with increasing dissolution. Nonetheless, face 3 clearly experiences a higher heterogeneity in rate distribution, due to the presence of macrosteps

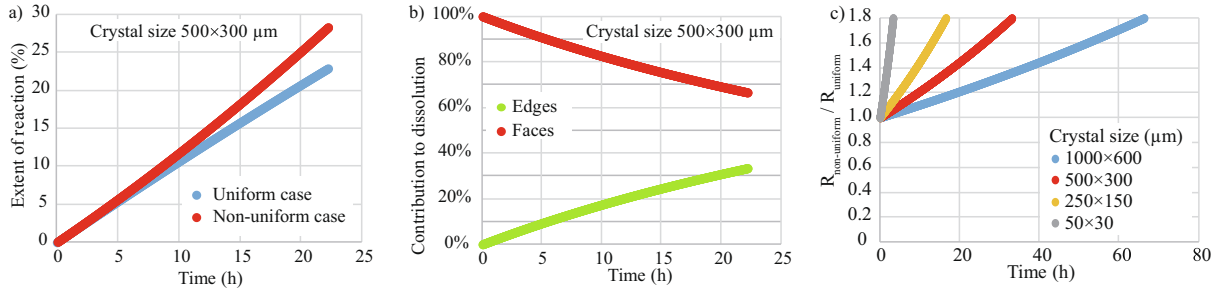

Fig. 14. (a–b) Outputs of the geometric model of calcite dissolution, for a 500 × 300 µm crystal size similar to the one investigated by XMT. (a) Evolution of the extent of reaction for uniform dissolution compared to non-uniform dissolution, where the enhanced dissolution at edges is accounted for. (b) Modeled contribution of edges and faces to the dissolution rate of calcite for the non-uniform case. (c) Modeled non-uniform over uniform ratio of calcite dissolution rates for various crystal sizes. See Appendix C for details of the calculations.

whose dissolution is enhanced at their top and reduced at their base. It is expected that the surface with higher energy will evolve to lower energy configuration (Smith et al., 2013). At the end of the experiment, the surface remains covered with rippled steps, except at some locations near the crystal edges (Fig. 9c), indicating that this low energy configuration has not been reached yet, despite an average surface retreat of about 22 µm.

Crystal defects that were created during the initial crystal crushing and size reduction also contribute to dissolution by increasing locally the dissolution rate. The dissolution rate along cleavages is clearly enhanced (Fig. 9c), anisotropic along the $[48\bar{1}]$ direction, and also might be limited by diffusion. This latter statement is supported by the observation that the depth of the deep cleavage shown in Fig. 7a does not increase between t_2 and t_3. In contrast, we can clearly see that the topography is affected in the vicinity of the cleavage, expanding the area of influence of the cleavage along the $[48\bar{1}]_+$ and $[48\bar{1}]_-$ directions, similarly to what can be observed at a smaller scale in etch pits, and at a larger scale at crystal edges. This is also visible for parting planes (Fig. 9b), although dissolution at parting plane is not anisotropic like at cleavages. However, discontinuities at their surface serve as well for trains of steps to initiate and propagate over the surface. These observations clearly show how sample preparation can infer on determination of the reaction rates, and that finely crushed crystals will experience higher dissolution rates due to a higher number of defects at the crystal surface and inside that favor step propagation over the crystal surface.

Comparison of local rates on cleaved faces interestingly shows that rates at etch pits are initially (i.e., between t_0 and t_1) faster than the average surface retreat (Fig. 11e). However, the trend is reversed afterwards (Fig. 11f). Noiriel et al., 2019 also observed the progressive disappearance of etch pits at constant pH 4.0 while their rate of formation was initially higher than the average face retreat, similarly to this study. The main assumption to explain this phenomenon arises from the increasing contribution of steps coming from the edges that take over the surface retreat by etch pit growth or spontaneous pit formation at the $\{10\bar{1}4\}$ surfaces. This is supported by the fact that the closer the etch pits to a crystal edge, the faster they disappear. However, dissolution in etch pits might also be limited by diffusion (Bouissonnié et al., 2018) or by changes in the dislocation line direction (Pollet-Villard et al., 2016b). In addition, the rate at the edges also increases comparatively more than the rate at the faces at pH 4.0 rather than at pH 4.5 (Fig. 12b,c and Fig. 11c,d), supporting that the contribution of the different crystal patterns to dissolution might also be pH-dependent.

4.5. XMT dissolution rate distributions

The distributions of measured local dissolution rates, as shown in Fig. 12, have an asymmetric shape, bell-type with a long tail, similar to what has been reported for calcite in the literature (Bibi et al., 2018; Brand et al., 2017; Fischer et al., 2012; Fischer et al., 2014; Noiriel et al., 2019). However, contrary to the distributions obtained from VSI, AFM or DHM on single faces, the distributions highlight here the contribution of all the crystal features to the dissolution process, including the crystal edges and corners, cleavages, parting planes, macro-steps, etch pits, flat $\{10\bar{1}4\}$ and misoriented surfaces, and topographic lows. However, it remains difficult to evaluate precisely the contribution of each feature due to the impossibility to clearly define their spatial extension, a soft transition being most likely observed between the edges, the faces and/or the other crystal features instead.

Deconvoluting the rate distribution also assumes that the local rates would be constant through time, a hypothesis not consistent with the experimental observations, e.g., the changes in the etch pits-to-surface or edge-to-surface retreat ratios with time. Fischer and Luttge, 2018 and Lüttge et al., 2019 have previously pointed at the spatial and temporal variability in surface reactivity, which should drive models of rate distribution to evolve to more probabilistic ones. These models will appear to be well adapted to better constrain the dissolution processes of crystals with different size, aspect ratio, density of defects at the surface and within the crystal, as all these parameters will contribute to modify the shape of the rate distribution. Indeed, a simple comparison of the local rate distribution for 11.1 h of experiment at pH 4.0 (i.e., between t_1 and t_2) with the results of Noiriel et al., 2019 after 12 h of experiment in the same pH and experimental conditions shows that the

rate distributions of the calcite crystals with two different aspect ratios do not match, although the rate at the peak maxima, the average rates ($\bar{r}'_{diss}$ equal to 1.43 μm h^{-1} in Noiriel et al., 2019 *vs* 1.34 μm h^{-1} in this study), and maximum rates at the edges fit very well (Fig. 15).

4.6. Does XMT have the ability to reconcile dissolution rates in the laboratory?

Compared to published data obtained in the same pH range (Fig. 16), the average surface normalized rates (Table 2) obtained with XMT are shown to be intermediate between the rates determined on calcite powders (Chou et al., 1989; Plummer et al., 1978) and the rates derived from AFM (De Giudici, 2002; Shiraki et al., 2000). The best agreement with previous studies corresponds to the rates obtained on macro-crystals (i.e., cm-size crystals) (Busenberg and Plummer, 1986; Sjöberg and Rickard, 1984, Schott et al., 1989), or from calcium released during dissolution of cleaved crystals of 2–3 mm in dimension and epoxy-resined to a glass base (Shiraki et al., 2000). The discrepancies between the rates are certainly explained by: (i) the procedure of normalization, and (ii) differences in experimental preparation and setup, as already discussed by Arvidson et al., 2003.

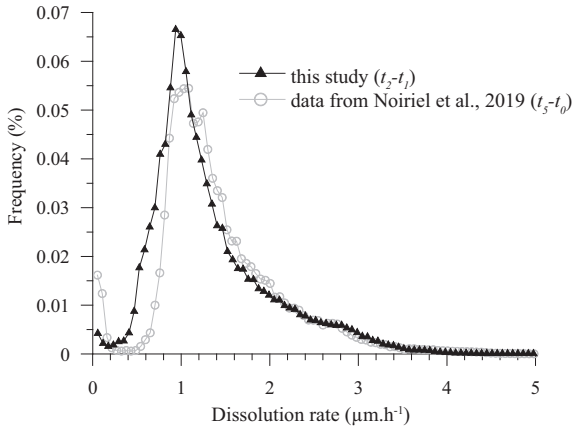

Fig. 15. Normalized histograms for two calcite crystals with different aspect ratios dissolved in similar experimental conditions (i.e., pH 4.0, Δt=11.5 h ± 0.5 h). See Noiriel et al., 2019 for more details about the geometry of the second crystal. Note that the image processing procedure to evaluate surface retreat was different in the two studies, so that the rates at the edges from Noiriel et al., 2019 should be slightly higher if the surface retreat was calculated normal to surface instead of normal to the closest {10 1 4} surface only.

A basic trend in the literature is confirmed that measured surface-normalized rates decrease as spatial resolution improves and the field of view decreases (Fig. 16). Considering geometric surface area as the normalization factor, these differences could be easily related to the spatial resolution of the imaging techniques, as the surface area scales with the resolution. Indeed, a finer resolution catches up more details of the surface topography, in relation with the surface roughness. This assumption is valid if we consider that the rates reported for the crystal used in this study are at least 1.6 times higher compared to the rates that would be determined on equivalent macro-crystals for which the contribution of edges and corners to the overall dissolution should be minimal. However, in this case, it would not explain why our results agree quite well rates obtained on macro-crystals (Busenberg and Plummer, 1986; Sjöberg and Rickard, 1984, Schott et al., 1989), unless we consider that normalization to a simple, geometric surface area calculated from the dimension and shape of the unreacted crystals could also lead to slight overestimation of the rates in experiments on macro crystals.

Of note, this scale-dependence of the surface area should not apply for rates determined from powder experiments which results are normalized to the BET surface area (Brunauer et al., 1938) instead. Some studies have reported BET surfaces areas about 2.5–3 times greater that geometric surface area for calcite crystals in the range 20–53 μm, 10–100 μm or 355–500 μm (Naviaux et al., 2018; Noiriel et al., 2019). In these experiments, in addition, the rates are normalized to the surface area determined on unreacted

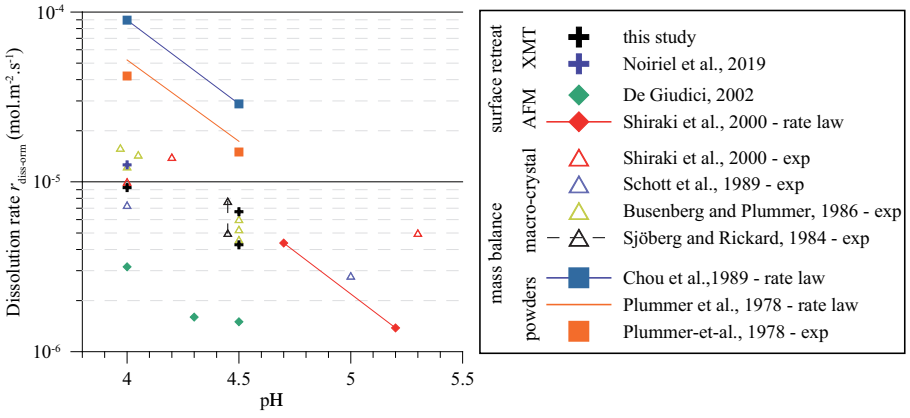

Fig. 16. Comparison between calcite dissolution rates (in HCl at pH 4–4.5) of the literature with this study. Both experimental data (exp) and derived models (rate law) are depicted. Rates are derived either from mass balance for crystal powders or cleaved macro-crystals of mm- to cm- size, or from surface retreat using AFM or XMT imaging.

minerals, whereas surface area is a dynamic parameter that evolves as the reaction progresses (Noiriel and Daval, 2017). The scale-dependence does not apply either for rates derived from direct measurements of the retreat velocity (μm h^{-1}) with AFM, VSI, DHM or XMT ($\bar{r}'_{diss}$), for which the rates are further normalized to the molar volume of the mineral, using Eq. (6). This method of normalization should be preferred, as it makes it possible to overcome the issues inherent to surface normalization by the geometric or the BET surface area. In this study, the rates normalized to the geometric surface area ($r_{diss-norm}$) slightly differ from the rates derived from the retreat velocity ($\bar{r}'_{diss-norm}$) (Table 2), but remains in quite good agreement, thus indicating that the geometric surface area derived from XMT at the μm-scale provides reliable estimation of the reactive surface area.

It is worth noting that normalization to the BET surface area would have reduced the rates by a factor of 2.7. Nevertheless, it is surprising that the rate laws obtained by Plummer et al., 1978 and Chou et al., 1989, which were derived from powder experiments (with crystal size in the range 177–420 μm, 420–841 μm, or 300–400 μm) and normalized to the geometric surface area are so high compared to the rate determined with XMT on crystals of comparable size (Fig. 16). Simple geometric considerations can show that the methods of normalization cannot account for such discrepancies, as for instance the specific surface area value of 44.5 cm^2 g^{-1} used by Plummer et al., 1978 for their 420–841 μm crystal size fraction fits well with our data.

As a consequence, the discrepancies must result from the sample preparation and/or from the experimental conditions. Indeed, crushed material will exhibit more surface micro-defects, micro-cracks, macro-steps, cleavages, parting planes, misoriented faces, and corners. Decreasing the size fraction by increasing the crushing intensity will increase the density of these features as well, thus promoting larger dissolution rates through a microstructural control of mineral reactivity. The presence of fine size particles not removed by sieving or acid washing could be an additional source of reactivity. In addition, contribution from the edges and corners to the dissolution rate will be enhanced as far as the size fraction decreases (Fig. 14c) by increasing the population of kink and step edge sites (Lüttge et al., 2013; Briese et al., 2017), thus also explaining larger rates compare to the XMT results. More importantly, the high stirring rates in the experiment of Chou et al., 1989 and Plummer et al., 1978 should contribute, as an extrinsic factor, in increasing the rates through transport control. For instance, Plummer et al., 1978 observed that, at pH 4, the rates were almost doubled between 800 and 1500 rpm. Similarly, Sjöberg and Rickard, 1984 observed, at pH 4.5, that the dissolution rate of a rotating macro-crystal was increased by a factor of 1.5 between 200 and 400 rpm (Fig. 16). Taken together, these various processes account for the discrepancies between the crystal powder experiments of Chou et al., 1989; Plummer et al., 1978 and the higher rates derived from XMT.

Similarly, face-specific (i.e., with little or no contribution of the edges) rates derived from AFM, VSI or DHM on small portions of flat surfaces with lower reactivity (Dove and Platt, 1996) will exhibit lower rates compared to the overall rate of crystals determined by other methods. For instance, Shiraki et al., 2000 observed, during dissolution of cleaved crystal of 2–3 mm in dimension and the sides of which were epoxy-coated, that the calcium fluxes normalized to the geometric surface were about a factor of 3 higher than the rates determined by AFM at all pH values. In addition, ignoring the contribution of the edges will contribute to increasing the underestimation of the overall rates.

4.7. Implications for mineral reactivity in the environment

Although most studies on the effects of weathering or hydrothermal alteration on minerals have focused on pit formation and morphology at the mineral surface (Berner et al., 1980; Velbel, 2009), several observations also mention the rounding of crystal edges in naturally weathered rocks (e.g., Velbel, 2009; Zhu et al., 2006) or experimentally altered crystals (e.g., Hellmann et al., 2010; Iwasaki and Sano, 1997; Saldi et al., 2017), supporting the idea that the edges will play a non-negligible role in the mass balance of alteration in various geochemical conditions. It is interesting to note that the geometry of altered grains will reflect the influence of the free energy of reaction ΔG_r. For instance, Hellmann et al., 2010 observed for albite that geometric etch pits and angular edges formed below a critical value of free energy of reaction ($\Delta G_r < \Delta G_r^{crit}$), whereas irregular pitting and rounded edges were observed at conditions $\Delta G_r > \Delta G_r^{crit}$. For calcite, no pit formation is expected above a critical undersaturation ($\Omega > 0.41$–0.54, Teng, 2004), so that the crystal edges should be assumed to play a major role in global calcite reactivity near equilibrium.

From a geologic perspective, the observations of higher crystal edge and corner reactivity in calcite have also far-reaching implications for reactive transport in carbonate reservoirs or aquifers, as geochemical reactivity should be linked to the rock fabric. Indeed, after carbonate diagenesis (e.g., burial, marine or meteoric diagenesis), it is common to observe coatings of fibrous, bladed or equant spar cements around grains (e.g., Flügel, 2010; Scholle and Ulmer-Scholle, 2006), whose crystal edges and corners are directly in contact with advective fluids. Preferential dissolution at the edges and corners of these cements could rapidly lead to pore roughness decrease (Fig. 17a), thus affecting the rock permeability (e.g., Noiriel et al., 2005; Noiriel et al., 2016). Conversely, for encasing cements, e.g. drusy mosaic of equant spar, the whole perimeter edge of the crystals (i.e., the grain boundaries) is in contact with fluids. It could be advocated that transport would remain long diffusion-limited in these micro-porous networks compare to larger pores where transport is advective, but if dissolution is favored at the crystal edges, and considering that corners and edges form the primary interconnected flow paths in many rocks (Lee et al., 1991), this also could enhance the creation of new flowpaths along the crystal edges (Fig. 17b), thus explaining why the global reactivity can be rapidly increased in some limestones, as shown for

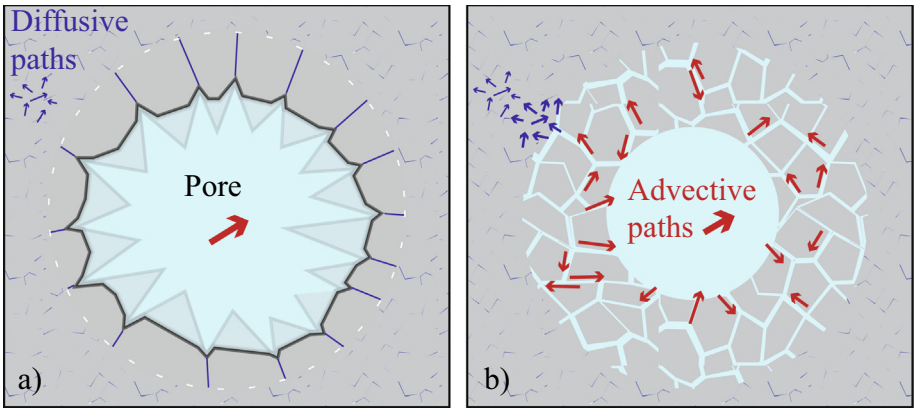

Fig. 17. Possible effect of preferential dissolution at the crystal edges and corners in carbonate rocks. (a) Pore roughness reduction due to preferential dissolution of coatings of equant spar cement grown in a pore. (b) Increase of diffusivity and mass transfer in micro-porous encasing cement due to preferential dissolution at the crystal edges.

instance in the reactive flow experiment of Noiriel et al., 2009. As a consequence, the quantitative estimation of the reactivity of crystal edges and corners appears as crucial data to upscale mineral reactivity in porous media, which may ultimately be used in reactive transport codes to model the modification of rock geometry and fluid flow paths.

5. CONCLUSION

Exploring the dissolution of a single crystal of calcite in full 3D at the sub-micron scale has revealed how the constitutive elements of the crystal with higher kink and step densities, i.e. the edges and corners, as well as the patterns resulting from sample crushing and size reduction, i.e., cleavages, parting planes, miscut r-plane faces or other surface defects are associated to faster surface retreat, and so higher dissolution rates compared to those with low surface energy morphologies, i.e. flat $\{10\bar{1}4\}$ surfaces and topographic lows.

Far from equilibrium and under acidic conditions, the highest rates measured at the crystal corner and edges are up to 7.2 and 2.1 times higher in average than the average face retreat, resulting in dissolution rate enhanced by a factor of at least ~1.6 compared to what would be a face-specific dissolution ignoring the contribution of the edges. The crystal edges take progressively control of the dissolution process, with trains of steps propagating and progressively invading the initially well-cleaved $\{10\bar{1}4\}$ surfaces, thus obliterating the face-specific retreat, with the consequence of pit progressive annihilation. The results clearly show that the crystal edges play a major role in the dissolution process of sub-millimeter scale calcite crystals. The contribution of the edges to dissolution will be even promoted as far as the crystal size decreases, thus explaining why dissolution rates determined on crystal powders scale with the crystal size distribution decrease. The results obtained from a simple geometric model generalize, at the sub-millimeter scale, the results of Briese et al., 2017 on nm-scale cubic crystals obtained from KMC simulations. The crystal aspect ratio is another parameter which should be considered, as the faces with the shortest dimensions should also experience a greater contribution from the edges.

With the perspective of determining reliable rates, these results should have implications for modeling of dissolution or reactive transport in well crystallized carbonates. The results also demonstrate that, despite a lower resolution compared to other techniques measuring the surface retreat, XMT is very well adapted to evaluate the contribution of any of the different patterns that are heterogeneously distributed at the crystal surface and through depth in course of dynamic experiments and for different fluid compositions, both on the long term and independently of the surface geometry or orientation. All considered, XMT appears to be helpful to provide reliable reaction rates and to fill the gap between fine-scale (nm- to μm-scale) measurements of surface reactivity and macroscopic determination of rates, a first necessary step toward bridging the gap between field and laboratory rates. Our study has shown that ignoring the contribution of the crystal edges as well as increasing the number of defects of higher reactivity via crushing at the surface compared to flat, well-cleaved or polished surfaces can be source of large discrepancies between the different approaches adopted so far in the laboratory. The origin of the largest rates determined from powder experiments –up to one order of magnitude-, however, is not fully resolved. In any case, it seems that these rates largely overestimate the reactivity of calcite at low pH values.

Data availability statement

Details of analyses on aqueous samples and the 3D crystal geometry of the sub-sampled volumes after segmentation can be found online at: https://doi.org/10.17632/hfg4w9hvsw.1

Declaration of Competing Interest

The authors declare that they have no known competing financial interests or personal relationships that could have appeared to influence the work reported in this paper.

ACKNOWLEDGMENTS

This work was funded by the Institut Carnot ISIFOR under project SEQFRAC 400034. We acknowledge the Paul Scherrer Institute for provision of synchrotron radiation beamtime at Swiss Light Source, TOMCAT beamline X02DA. Local contacts David Haberthür and Iwan Jerjen are acknowledged for their assistance with image acquisition. We also thank Thierry Aigouy for assistance with SEM imaging.

APPENDIX A. UNCERTAINTY IN XMT ANALYZED DATA

The error in determining the fluid-crystal interface, crystal volume and reaction rates from XMT imaging depends on several factors including the acquisition parameters, X-ray beam stability, crystal properties, image noise-to-signal ratio, and image processing. Consequently, the error from XMT is not easily quantifiable (Noiriel et al., 2007). Nevertheless, the error can be estimated by comparison either with other measurement techniques (e.g. VSI topography measurements, which vertical resolution is 2–3 nm) or with model data for which the uncertainty is constrained by visual observations on the data sets.

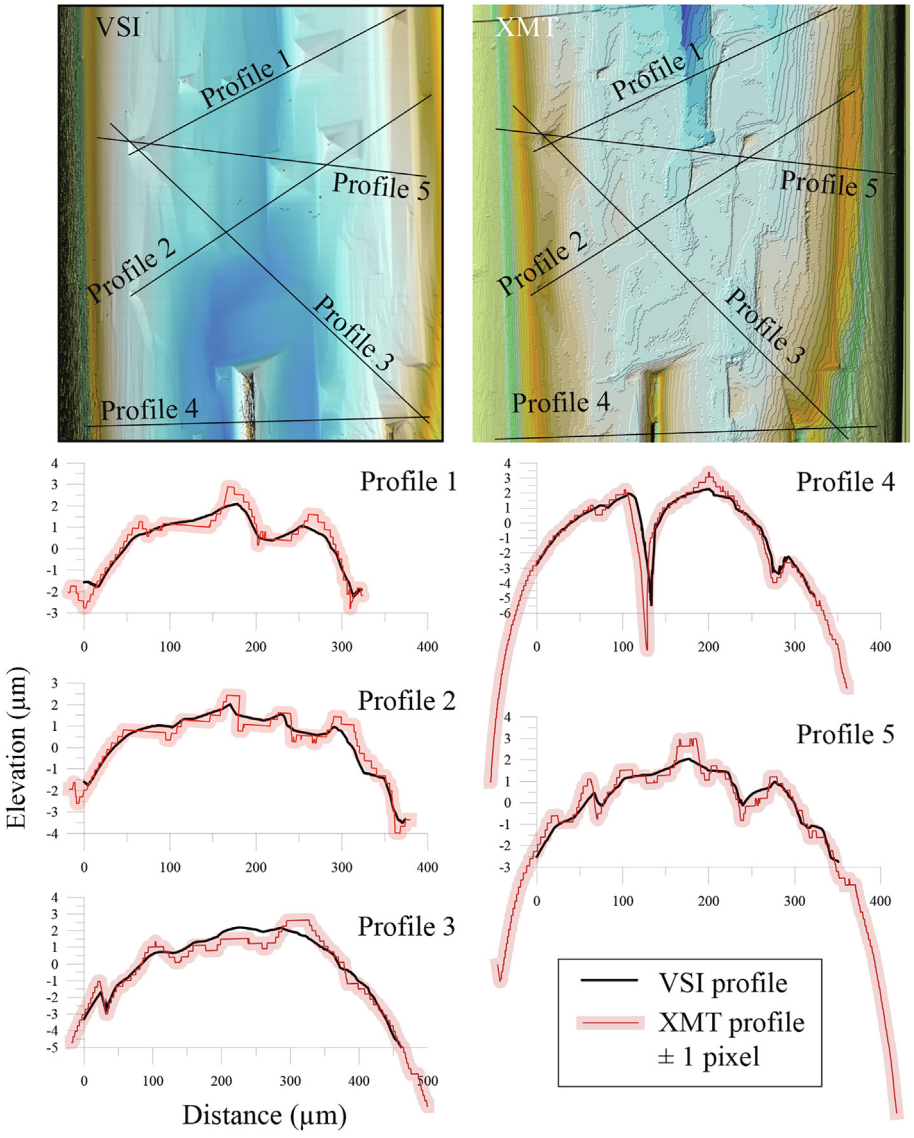

Fig. A1. Comparison of VSI and XMT profiles from face 1. The profiles are identified on the corresponding images. For XMT profiles, the line thickness corresponds to an error bar of ±1 pixel (0.325 µm). Note that the profiles are not fully identical due to the difficulty in positioning the profiles on images with different resolutions.

A.1. Error on the positioning of the fluid-crystal interface

Assuming that the uncertainty in the fluid-crystal interface positioning is one pixel of the face extracted in the VOIs, the resulting error would be ±0.325 µm. To verify this assumption, several 1D profiles from XMT topography maps were compared with VSI profiles at about the same location. Fig. A.1 shows the results for five XMT and VSI profiles registered in the same coordinate systems, as their corresponding position on the VSI and XMT maps at the surface of face 1 at t_3. The profiles depict similar topography trends, but XMT seems to overestimate the position of the fluid-mineral interface at high elevations. This phenomenon certainly arises from the presence of star artifacts at the surface of topographic highs, with the consequence of overestimating the elevation during segmentation, the bright pixels of the artifacts at the surface of the crystal (i.e., in the air phase) being confused with solid pixels (i.e., pixels belonging to the crystal). However, there is a high degree of consistency between the profiles, and 1 pixel error seems a reasonable assumption.

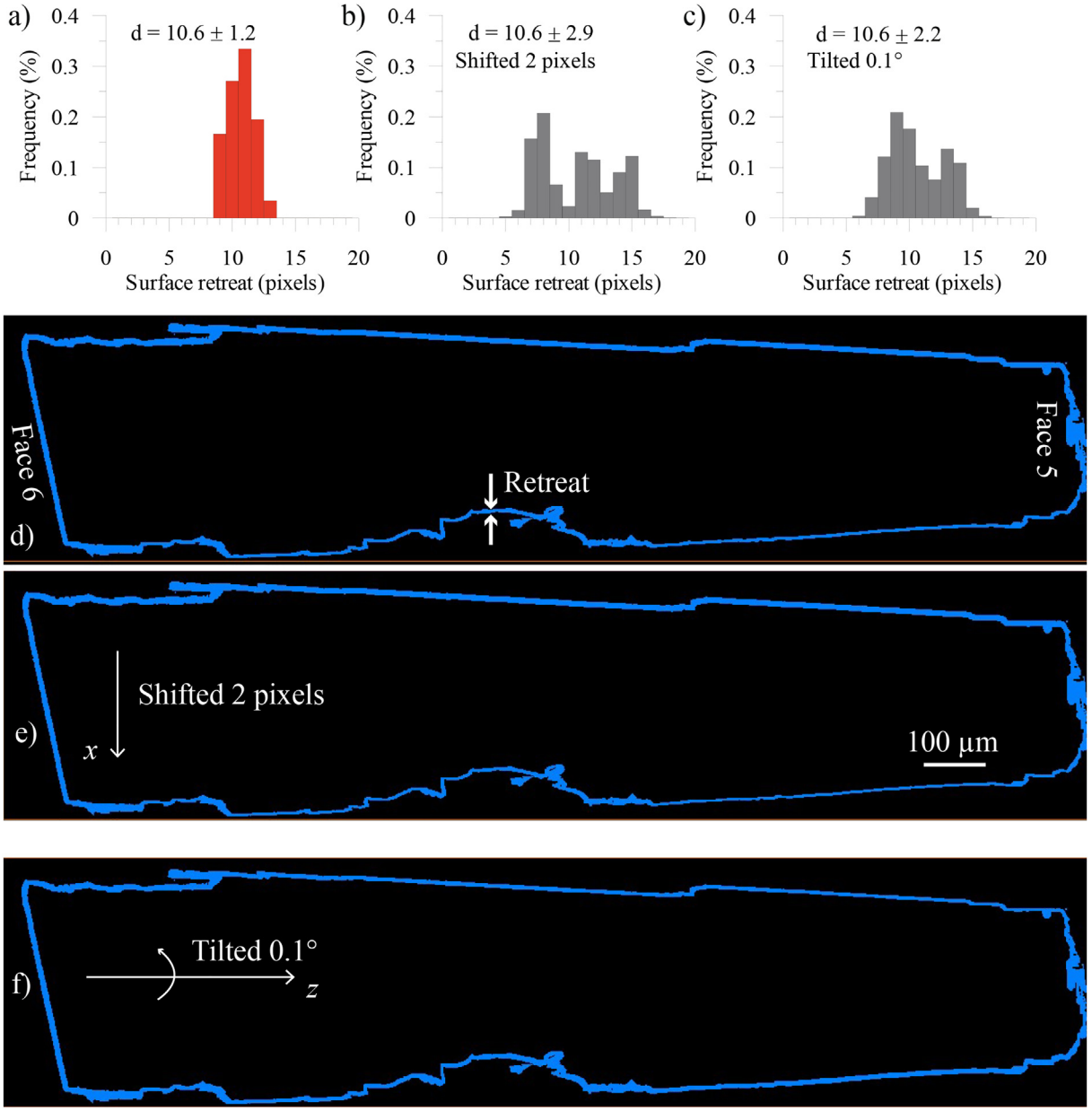

Fig. A2. Effects of possible misregistration on the surface retreat distribution between two stages of dissolution. (a) Uniform distribution resulting from a 10-pixel erosion filter of the unreacted crystal. (b) Distribution obtained after a 2-pixel translation of the crystal in the x-direction. (c) Distribution obtained after a 0.1° rotation along the z-axis. (d)–(f) Corresponding retreat, in blue (view in cross-section), corresponding to the difference between the unreacted crystal and (d) the crystal eroded, (e) the crystal eroded and shifted or (f) tilted.

A.2. Error on the crystal volume determination

Assuming that the uncertainty in the fluid-crystal interface positioning is again one pixel, the error would be ±0.65 µm on the segmented images, as the data sets were resampled by a factor of 2 to reduce the file sizes. To evaluate the effect on the crystal volume determination, the volume of the crystal was recalculated by either removing or adding 1 pixel at the crystal surface with a 3D erosion or dilation filter (with a 6 pixel-coordination). The maximum relative error on the crystal volume determination that way is 0.74%. The corresponding error bars on $\Delta n_{calcite-XMT}$ determination are shown in Fig. 10.

A.3. Error on the local rate determination

The major factor contributing to uncertainties in the dissolution rate determination at the crystal surface arises from misregistration of the XMT volumes between the different stages of the experiment. The worst scenario of misregistration, i.e., the maximal error values without which misregistration can be noticed by visual inspection of the superimposed crystals or crystal marks inside the crystal structure, would correspond to a translation of the crystal of two pixels horizontally, mostly resulting from a maximum vertical tilt of the crystal of 0.1°.

The error induced by misregistration of the 3D data sets was quantified by examining the effect of crystal translation

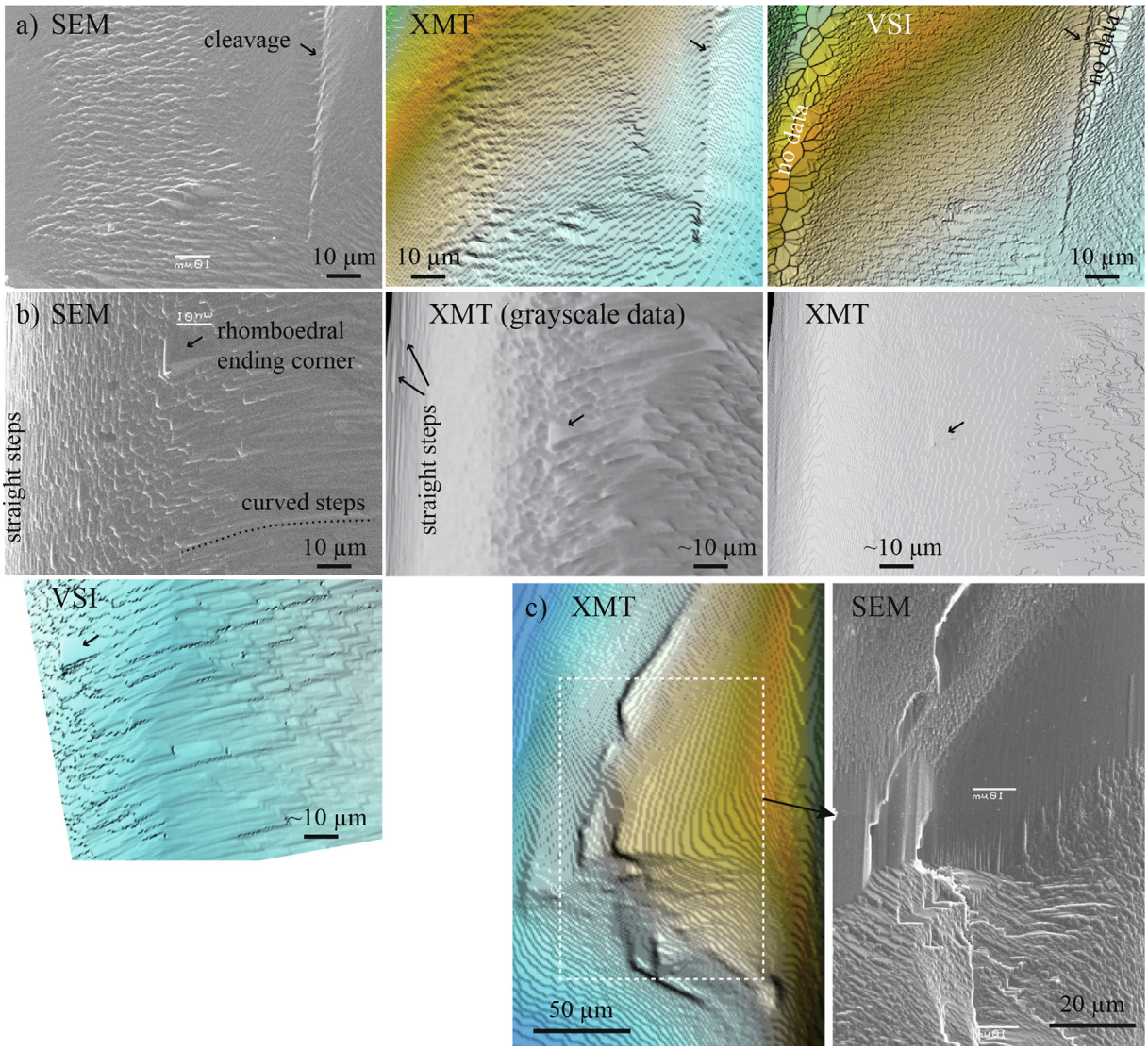

Fig. B1. Selected images from XMT and SEM, and VSI surfaces. (a) Detail of the stepped surface near the cleavages of face 3. The mosaic patterns on the VSI maps results from interpolation, meaning that there was no data measured by the interferometer in these areas with steep changes in the topography. (b) Rhombohedral ending corners at the junction between straight steps and curved steps at the crystal edge 2–3. The rhomboedral corner is visible on the XMT segmented image, although more visible on the grayscale data set. (c) Topographical low near the edge 2–3. Note that all the images are flipped horizontally.

and rotation on the rate distribution. To explore these effects, a new crystal was created from the unreacted crystal by removing 10 pixels at the surface with a 3D erosion filter (18 pixel-coordination). The resulting crystal was compared to the original one to examine the retreat at the surface using the same procedure as described in Section 2.3.4 to calculate the surface retreat distribution. As expected, the surface retreat of the eroded crystals is quasi-uniform, with an average surface retreat of 10.6 ± 1.2 pixels. Then, the resulting crystal was applied either (i) a translation of the crystal of two pixels horizontally, or (ii) a vertical tilt of the crystal of 0.1°. The results are shown in Fig. A2. The misregistration does not change the average surface retreat, but clearly affect both the shape of the surface retreat distributions and the standard deviation. The shape of the surface retreat distributions becomes bimodal, whereas the standard deviation increases from to 1.2 to 2.9 and 2.2. It is expected that the misfit of the sub-volumes results in an increase of the standard deviation of the surface retreat, thus slightly affecting the distribution of the local dissolution rates.

APPENDIX B. QUALITATIVE IMAGE COMPARISON

Additional views of XMT, SEM and VSI are provided (Fig. B1).

APPENDIX C. MODEL OF CRYSTAL DISSOLUTION

Let us consider a rhombohedron made of six $\{10\bar{1}4\}$ faces, with a fixed height H_0 (Fig. C1). This geometry is similar to the case of the experiment, where the studied crystal has one basal face that is masked. Here, for the sake of simplicity, we assume that the opposite face is similarly masked.

Case #1: Uniform dissolution of the crystal faces

Here, it is assumed that the reactivity of edges does not exceed the reactivity of the faces. The temporal evolution of the surface area (S) of the projected parallelogram of length L, width l, and height h is given by:

$$S(t) = L(t) \times h(t) \tag{C.1}$$

If α corresponds to the acute angle of the parallelogram (78°) and r_{104} (m s^{-1}) is the surface retreat rate in the direction normal to each $\{10\bar{1}4\}$ face, then $S(t)$ can be written following:

$$S(t) = (L_0 - 2r_{104}.t/\sin(\alpha)).(h_0 - 2r_{104}.t) \tag{C.2}$$

where L_0 and h_0 are the length and height of the parallelogram at $t = 0$. The dissolution rate of the whole crystal (mol s^{-1}) can simply be calculated following:

$$R_{uniform} = \frac{dn}{dt} = -\frac{dS}{dt} \times \frac{H_0}{v_{calcite}} = -\frac{H_0}{v_{calcite}} \times \left(-2r_{104}L_0 - \frac{2r_{104}h_0}{\sin(\alpha)} + \frac{8\,r_{104}^2}{\sin(\alpha)} \times t\right) \tag{C.3}$$

The normalized extent of reaction is then given by:

$$\xi_{uniform}(t) = 100\frac{S_0 - S(t)}{S_0} \tag{C.4}$$

Case #2: Non-uniform dissolution

Here, it is assumed that the reactivity of edges exceeds the reactivity of the faces. This specific reactivity will lead to the progressive development of facets that will grow in the direction normal to the bisectors of the angles of the considered parallelogram. For the uniform dissolution configuration, the distance between the initial position of the edge and its position at time t is given by:

$$d_{uniform}(t) = \frac{2r_{104}}{\sin(\alpha/2)}t \tag{C.5}$$

For the non-uniform case, this distance becomes:

$$d_{non-uniform}(t) = \gamma \times d_{uniform}(t) \tag{C.6}$$

where γ is a constant equal to ~2.4 according to the experimental results. The surface of the growing triangle that represents the additional surface that is dissolved at each edge of the projected parallelogram can then be written:

$$S_{triangle}(t) = \left(\frac{r_{104}t}{\sin(\alpha/2)}\right)^2 \times \tan(\alpha/2) \times (\gamma - 1)^2 \tag{C.7}$$

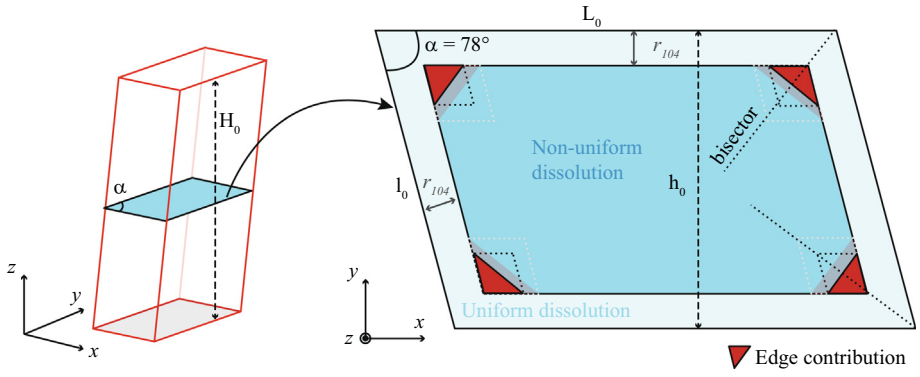

Fig. C1. Model of uniform (light blue) *vs* non-uniform (blue) dissolution of the crystal faces, including extra dissolution at the crystal edges (in red) in the non-uniform case. (For interpretation of the references to colour in this figure legend, the reader is referred to the web version of this article.)

Following simple geometric considerations, it is easy to demonstrate that this surface is the same for all triangles arising from the four edges of the parallelogram. Then, the overall dissolution rate can be written following:

$$R_{non-uniform} = -\frac{H_0}{v_{calcite}} \times \left(-2r_{104}L_0 - \frac{2r_{104}h_0}{\sin(\alpha)} + \left(\frac{8\,r_{104}^2}{\sin(\alpha)} - \frac{8\,r_{104}^2 \tan(\alpha/2) \times (\gamma-1)^2}{\sin(\alpha/2)^2} \right) \times t \right) \quad \text{(C.8)}$$

And the extent of reaction becomes:

$$\xi_{non-uniform}(t) = 100\frac{S_0 - S(t) + 4S_{triangle}(t)}{S_0} \quad \text{(C.9)}$$

Note that these estimations remain valid as long as the triangles do not intersect in the area defined by the uniformly dissolved parallelogram at time t. We made sure that all the figures reported in the manuscript observe this criterion.

Finally, the respective contribution of faces and edges to the dissolution rate can be conveniently described using the following criteria:

$$\gamma_{face} = \frac{R_{uniform}}{R_{non-uniform}} \quad \text{(C.10)}$$

$$\gamma_{edge} = \frac{R_{non-uniform} - R_{uniform}}{R_{non-uniform}} \quad \text{(C.11)}$$

REFERENCES

Akmal Butt M. and Maragos P. (1998) Optimum design of chamfer distance transforms. *Image Process., IEEE Trans.* **7**, 1477–1484.

Akutsu N. (2014) Pinning of steps near equilibrium without impurities, adsorbates, or dislocations. *J. Cryst. Growth* **401**, 72–77.

Arvidson R. S., Evren Ertan I., Amonette J. E. and Lüttge A. (2003) Variation in calcite dissolution rates: A fundamental problem?. *Geochim. Cosmochim. Acta* **67** 1623–1634.

Arvidson R. S., Beig M. S. and Lüttge A. (2004) Single-crystal plagioclase feldspar dissolution rates measured by vertical scanning interferometry. *Am. Miner.* **89**, 51–56.

Arvidson R. S., Collier M., Davis K. J., Vinson M. D., Amonette J. E. and Lüttge A. (2006) Magnesium inhibition of calcite dissolution kinetics. *Geochim. Cosmochim. Acta* **70**, 583–594.

Berner R. A., Sjoberg E. L., Velbel M. A. and Krom M. D. (1980) Dissolution of pyroxenes and amphiboles during weathering. *Science* **207**, 1205–1206.

Bibi I., Arvidson R. S., Fischer C. and Luttge A. (2018) Temporal evolution of calcite surface dissolution kinetics. *Minerals* **8**, 256.

Bisschop J., Dysthe D. K., Putnis C. V. and Jamtveit B. (2006) In situ AFM study of the dissolution and recrystallization behaviour of polished and stressed calcite surfaces. *Geochim. Cosmochim. Acta* **70**, 1728–1738.

Bonzel H. P. (2003) 3D equilibrium crystal shapes in the new light of STM and AFM. *Phys. Rep.* **385**, 1–67.

Bouissonnié A., Daval D., Marinoni M. and Ackerer P. (2018) From mixed flow reactor to column experiments and modeling: Upscaling of calcite dissolution rate. *Chem. Geol.* **487**, 63–75.

Brand A. S., Feng P. and Bullard J. W. (2017) Calcite dissolution rate spectra measured by in situ digital holographic microscopy. *Geochim. Cosmochim. Acta* **213**, 317–329.

Bras W. and Stanley H. (2016) Unexpected effects in non crystalline materials exposed to X-ray radiation. *J. Non-Cryst. Solids* **451**, 153–160.

Briese L., Arvidson R. S. and Luttge A. (2017) The effect of crystal size variation on the rate of dissolution : A kinetic Monte Carlo study. *Geochim. Cosmochim. Acta* **212**, 167–175.

Brunauer S., Emmet P. H. and Teller E. A. (1938) Adsorption of gases in multimolecular layers. *J. Am. Chem. Soc.* **60**, 309–319.

Busenberg E. and Plummer L. N. (1986) A comparative study of the dissolution and precipitation kinetics of calcite and aragonite. In *Studies in Diagenesis* (ed. F. A. Mumton). U. S Geological Survey Bulletin.

Chen J. C., Reischl B., Spijker P., Holmberg N., Laasonen K. and Foster A. S. (2014) Ab initio Kinetic Monte Carlo simulations of dissolution at the NaCl-water interface. *Phys. Chem. Chem. Phys.* **16**, 22545–22554.

Chou L., Garrels R. M. and Wollast R. (1989) Comparative study of the kinetics and mechanisms of dissolution of carbonate minerals. *Chem. Geol.* **78**, 269–282.

Daval D., Hellmann R., Saldi G. D., Wirth R. and Knauss K. G. (2013) Linking nm-scale measurements of the anisotropy of silicate surface reactivity to macroscopic dissolution rate laws: New insights based on diopside. *Geochim. Cosmochim. Acta* **107**, 121–134.

De Giudici G. (2002) Surface control vs. diffusion control during calcite dissolution: Dependence of step-edge velocity upon solution pH. *Am. Miner.* **87**, 1279–1285.

DePaolo D. J. and Orr F. M. (2008) Geoscience research for our energy future. *Phys. Today* **61**, 46–51.

Dove P. M. and Platt F. M. (1996) Compatible real-time reaction rates for in situ imaging of mineral-water interactions using scanning force microscopy. *Chem. Geol.* **127**, 331–338.

Duckworth O. W. and Martin S. T. (2004) Dissolution rates and pit morphologies of rhomoedral carbonate minerals. *Am. Miner.* **89**, 554–563.

Emmanuel S. (2014) Mechanisms influencing micron and nanometer-scale reaction rate patterns during dolostone dissolution. *Chem. Geol.* **363**, 262–269.

Fenter P., Geissbühler P., DiMasi E., Strajer G., Sorenssen L. B. and Sturchio N. C. (2000) Surface speciation of calcite observed in situ by high-resolution X-ray reflectivity. *Geochim. Cosmochim. Acta* **64**, 1221–1228.

Fischer C., Arvidson R. S. and Lüttge A. (2012) How predictable are dissolution rates of crystalline material? *Geochim. Cosmochim. Acta* **98**, 177–185.

Fischer C., Kurganskaya I., Schaefer T. and Lüttge A. (2014) Variability of crystal surface reactivity: What do we know? *Appl. Geochem.* **43**, 132–157.

Fischer C. and Lüttge A. (2007) Converged surface roughness parameters - A new tool to quantify rock surface morphology and reactivity alteration. *Am. J. Sci.* **307**, 955–973.

Fischer C. and Lüttge A. (2018) Pulsating dissolution of crystalline matter. *Proc. Natl. Acad. Sci.*.

Flügel E. (2010) *Microfacies of Carbonate Rocks: Analysis, Interpretation and Application*. Springer.

Godinho J. R. A., Piazolo S. and Evins L. Z. (2012) Effect of surface orientation on dissolution rates and topography of CaF2. *Geochim. Cosmochim. Acta* **86**, 392–403.

Gonzales R. C. and Woods R. E. (1992) *Digital image processing*. Addison-Wesley Publishing Compagny, Reading, Massachusetts.

Hellmann R., Daval D. and Tisserand D. (2010) The dependence of albite feldspar dissolution kinetics on fluid saturation state at acid and basic pH: Progress towards a universal relation. *C.R. Geosci.* **342**, 676–684.

Hillner P. E., Gratz A. J., Manne S. and Hasma P. K. (1992) Atomic-scale imaging of calcite growth and dissolution in real time. *Geology* **20**, 359–362.

Hochella M. F. J. (1990) *Atomic strucutre, microtopography, composition and reactivity of mineral surfaces*. Mineral-Water Interface Geochemistry.

Iwasaki A. and Sano T. (1997) Dissolution behavior of silicalite crystal. *Zeolites* **19**, 41–46.

Jordan G. and Rammensee W. (1998) Dissolution rates of calcite (10(1)over-bar4) obtained by scanning force microscopy: Microtopography-based dissolution kinetics on surfaces with anisotropic step velocities. *Geochim. Cosmochim. Acta* **62**, 941–947.

Kump L. R., Brantley S. L. and Arthur M. A. (2000) Chemical, weathering, atmospheric CO2, and climate. *Annu. Rev. Earth Planet. Sci.* **28**, 611–667.

Laanait N., Callagon E. B. R., Zhang Z., Sturchio N. C., Lee S. S. and Fenter P. (2015) X-ray–driven reaction front dynamics at calcite-water interfaces. *Science* **349**, 1330–1334.

Lee V. W., Mackwell S. J. and Brantley S. L. (1991) The effect of fluid chemistry on wetting textures in novaculite. *J. Geophys. Res.* **96**, 10023–10037.

Lüttge A., Winkler U. and Lasaga A. C. (2003) An interferometric study of dolomite dissolution: A new conceptuel model for mineral dissolution. *Geochim. Cosmochim. Acta* **67**, 1099–1116.

Lüttge A., Arvidson R. S. and Fischer C. (2013) A stochastic treatment of crystal dissolution kinetics. *Elements* **9**, 183–188.

Lüttge A., Arvidson Rolf S., Fischer C. and Kurganskaya I. (2019) Kinetic concepts for quantitative prediction of fluid-solid interactions. *Chem. Geol.* **504**, 216–235.

Maes F., Collignon A., Vandermeulen D., Marchal G. and Suetens P. (1997) Multimodality image registration by maximization of mutual information. *IEEE Trans. Med. Imaging* **16**, 187–198.

Marone F. and Stampanoni M. (2012) Regridding reconstruction algorithm for real-time tomographic imaging. *J. Synchrotron Radiat.* **19**, 1029–1037.

Meijering E. H. W., Niessen W. J. and Viergever M. A. (2001) Quantitative evaluation of convolution-based methods for medical image interpolation. *Med. Image Anal.* **5**, 111–126.

Miyata K., Tracey J., Miyazawa K., Haapasilta V., Spijker P., Kawagoe Y., Foster A. S., Tsukamoto K. and Fukuma T. (2017) Dissolution processes at step edges of calcite in water investigated by high-speed frequency modulation Atomic Force Microscopy and simulation. *Nano Lett.* **17**, 4083–4089.

Morse J. W. and Arvidson R. S. (2002) The dissolution kinetics of major sedimentary carbonate minerals. *Earth Sci. Rev.* **58**, 51–84.

Naviaux J. D., Subhas A. V., Rollins N. E., Dong S., Berelson W. M. and Adkins J. F. (2018) Temperature dependence of calcite dissolution kinetics in seawater. *Geochim. Cosmochim. Acta* **246**, 363–384.

Noiriel C., Bernard D., Gouze P. and Thibaut X. (2005) Hydraulic properties and microgeometry evolution in the course of limestone dissolution by CO_2-enriched water. *Oil Gas Sci. Technol.* **60**, 177–192.

Noiriel C. and Daval D. (2017) Pore-scale geochemical reactivity associated with CO_2 storage: New frontiers at the fluid-solid interface. *Acc. Chem. Res.* **50**, 759–768.

Noiriel C., Madé B. and Gouze P. (2007) Impact of coating development on the hydraulic and transport properties in argillaceous limestone fracture. *Water Resour. Res.* **43**, W09406. https://doi.org/10.1029/2006WR005379.

Noiriel C., Luquot L., Madé B., Raimbault L., Gouze P. and van der Lee J. (2009) Changes in reactive surface area during limestone dissolution: An experimental and modelling study. *Chem. Geol.* **265**, 160–170.

Noiriel C., Steefel C. I., Yang L. and Ajo-Franklin J. (2012) Upscaling calcium carbonate precipitation rates from pore to continuum scale. *Chem. Geol.* **318–319**, 60–74.

Noiriel C., Steefel C. I., Yang L. and Bernard D. (2016) Effects of pore-scale heterogeneous precipitation on permeability and flow. *Adv. Water Resour.* **95**, 125–137.

Noiriel C., Oursin M., Saldi G. D. and Haberthür D. (2019) Direct determination of dissolution rates at crystal surface using 3D X-ray micro-tomography. *Earth Space Chem.* **3**, 101–108.

Parkhurst, D. L. and Appelo, C. A. J., 2013. Description of input and examples for PHREEQC version 3–A computer program for speciation, batch- reaction, one-dimensional transport, and inverse geochemical calculations, Techniques and Methods 6-A43, available only at http://pubs.usgs.gov/tm/06/a43. U.S. Geological Survey

Pitas I. (2000) *Digital image processing algorithms and applications*. Wiley.

Plummer L. N., Wigley T. M. L. and Parkhurst D. L. (1978) The kinetics of calcite dissolution in CO_2-water systems at 5° to 60° C and 0.0 to 1.0 atm CO_2. *Am. J. Sci.* **278**, 179–216.

Pollet-Villard M., Daval D., Ackerer P., Saldi G. D., Wild B., Knauss K. G. and Fritz B. (2016a) Does crystallographic anisotropy prevent the conventional treatment of aqueous mineral reactivity? A case study based on K-feldspar dissolution kinetics. *Geochim. Cosmochim. Acta* **190**, 294–308.

Pollet-Villard M., Daval D., Fritz B., Knauss K. G., Schäfer G. and Ackerer P. (2016b) Influence of etch pit development on the surface area and dissolution kinetics of the orthoclase (001) surface. *Chem. Geol.* **442**, 148–159.

Rickard D. and Sjöberg E. L. (1983) Mixed kinetic control of calcite dissolution rates. *Am. J. Sci.* **283**, 815–830.

Ruiz-Agudo E., Putnis C. V., Jiménez-López C. and Rodriguez-Navarro C. (2009) An atomic force microscopy study of calcite dissolution in saline solutions: The role of magnesium ions. *Geochem. Cosmochim. Acta* **73**, 3201–3217.

Russ J. C. (2011) *The Image Processing Handbook*, Sixth Edition. CRC Press, Boca Raton, FL.

Saldi G. D., Voltolini M. and Knauss K. G. (2017) Effects of surface orientation, fluid chemistry and mechanical polishing on the variability of dolomite dissolution rates. *Geochim. Cosmochim. Acta* **206**, 94–111.

Scholle P. A. and Ulmer-Scholle D. S. (2006) *Color Guide to Petrography of Carbonate Rocks*. AAPG.

Schott J., Brantley S. L., Drear D., Guy C., Borcsik M. and Willaime C. (1989) Dissolution kinetics of strained calcite. *Geochim. Cosmochim. Acta* **53**, 373–382.

Shiraki R., Rock P. A. and Casey W. H. (2000) Dissolution kinetics of calcite in 0.1M NaCl solution at room temperature: An atomic force microscopic (AFM) study. *Aquat. Geochem.* **6**, 87–108.

Sjöberg E. L. and Rickard D. T. (1984) Calcite dissolution kinetics: Surface speciation and the origin of the variable pH dependence. *Chem. Geol.* **42**, 119–136.

Smith M. E., Knauss K. G. and Higgins S. R. (2013) Effects of crystal orientation on the dissolution of calcite by chemical and microscopic analysis. *Chem. Geol.* **360**, 10–21.

Stampanoni, M., Groso, A., Isenegger, A., Mikuljan, G., Chen, Q., Bertrand, A., Henein, S., Betemps, R., Frommherz, U., Böhler, P., Meister, D., Lange, M., Abela, R., 2006. Trends in synchrotron-based tomographic imaging: the SLS experience. SPIE Optics + Photonics, 2006, San Diego, California, United States.

Steefel C. I., DePaolo D. J. and Lichtner P. C. (2005) Reactive transport modeling: An essential tool and a new research approach for the Earth sciences. *Earth Planet. Sci. Lett.* **240**, 539–558.

Stipp S. L. S., Eggleston C. M. and Nielsen B. S. (1994) Calcite surface observed at microtopographic and molecular scales with atomic force microscopy (AFM). *Geochim. Cosmochim. Acta* **58**, 3023–3033.

Teng H. H. (2004) Controls by saturation state on etch pit formation during calcite dissolution. *Geochim. Cosmochim. Acta* **68**, 253–262.

Ueta S., Satoh H., Nishimura Y., Ueda A. and Tsukamoto K. (2013) Dynamic and topographic observation of calcite dissolution using enhanced in-situ phase-shift interferometry. *J. Cryst. Growth* **363**, 294–299.

Velbel M. A. (2009) Dissolution of olivine during natural weathering. *Geochim. Cosmochim. Acta* **73**, 6098–6113.

Villanova J., Daudin R., Lhuissier P., Jauffrès D., Lou S., Martin C. L., Labouré S., Tucoulou R., Martinez-Criado G. and Salvo L. (2017) Fast in situ 3D nanoimaging: A new tool for dynamic characterization in materials science. *Mater. Today* **20**, 354–359.

Xu M., Hu X., Knauss K. G. and Higgins S. R. (2010) Dissolution kinetics of calcite at 50–70 °C: An atomic force microscopic study under near-equilibrium conditions. *Geochem. Cosmochim. Acta* **74**, 285–4297.

Zhu C., Veblen D. R., Blum A. E. and Chipera S. J. (2006) Naturally weathered feldspar surfaces in the Navajo Sandstone aquifer, Black Mesa, Arizona: Electron microscopic characterization. *Geochim. Cosmochim. Acta* **70**, 4600–4616.

Associate Editor: Lawrence M. Anovitz